

PONTIFICIA UNIVERSIDAD CATÓLICA DEL PERÚ

FACULTAD DE CIENCIAS E INGENIERÍA



**DEVELOPMENT AND IMPLEMENTATION OF A SHEAR WAVE
SPEED ESTIMATION ALGORITHM FOR CRAWLING WAVES
SONOELASTOGRAPHY**

Tesis para obtener el título profesional de Ingeniero Electrónico

AUTOR:

Mauricio Sebastian Merino Acuña

ASESORES:

Stefano Enrique Romero Gutierrez

Benjamin Castañeda Aphan

Lima, Septiembre, 2024


Informe de Similitud

Yo, Stefano Enrique Romero Gutierrez, docente de la Facultad de Ciencias e Ingeniería de la Pontificia Universidad Católica del Perú, asesor(a) de la tesis/el trabajo de investigación titulado “DEVELOPMENT AND IMPLEMENTATION OF A SHEAR WAVE SPEED ESTIMATION ALGORITHM FOR CRAWLING WAVES SONOELASTOGRAPHY” del autor Mauricio Sebastián Merino Acuña,

dejo constancia de lo siguiente:

- El mencionado documento tiene un índice de puntuación de similitud de 20%. Así lo consigna el reporte de similitud emitido por el software *Turnitin* el 01/10/2024.
- He revisado con detalle dicho reporte y la Tesis o Trabajo de Suficiencia Profesional, y no se advierte indicios de plagio.
- Las citas a otros autores y sus respectivas referencias cumplen con las pautas académicas.

Lugar y fecha: Lima, 02/10/2024

Apellidos y nombres del asesor / de la asesora: <u>Romero Gutierrez, Stefano Enrique</u>	
DNI: 46011069	 Firma
ORCID: https://orcid.org/0000-0001-6092-1395	

Resumen

La elastografía por ultrasonido es una técnica de imagen no invasiva cuyo objetivo es brindar información acerca de la elasticidad de los tejidos biológicos evaluando sus propiedades biomecánicas. Proporciona información valiosa sobre su rigidez, la cual está relacionada a los cambios biomecánicos ocasionados por condiciones patológicas. Esto la convierte en una herramienta valiosa para el diagnóstico y el seguimiento del tratamiento de enfermedades como el cáncer. Uno de los métodos de elastografía cuantitativa se basa en el uso de dos fuentes de vibración para generar un patrón de interferencia en el tejido. La onda de corte puede visualizarse en tiempo real mediante sonoelastografía y debe aplicarse un esquema de inversión para recuperar la velocidad de la onda de corte a partir de varios fotogramas. Sin embargo, los estimadores estudiados en la literatura exhiben algunas limitaciones tales como un pobre rendimiento en entornos ruidosos y prolongados tiempos de adquisición y procesamiento para aplicaciones en tiempo real.

En esta tesis se proponen e implementan dos algoritmos, basados en la transformada de Fourier de tiempo corto y la transformada Wavelet continua, para la estimación de la velocidad de la onda de corte. Se fabricaron maniquies homogéneos y heterogéneos de gelatina para evaluar el rendimiento de los algoritmos en condiciones controladas. Se realizaron experimentos de sonoelastografía a diferentes frecuencias de vibración para evaluar su precisión en una serie de escenarios. Los resultados demuestran que los algoritmos desarrollados son comparables a los estimadores existentes en términos de sesgo, coeficiente de variación, relación contraste-ruido y resolución. En medios homogéneos, el coeficiente de variación se mantuvo debajo del 10% para ambos estimadores y, en medios heterogéneos, la transformada Wavelet continua alcanzó una relación contraste-ruido de 30 dB en promedio. En general, los algoritmos muestran una robustez superior, sobre todo en presencia de una relación señal-ruido deficiente y en tejidos más rígidos con velocidades de onda de corte más

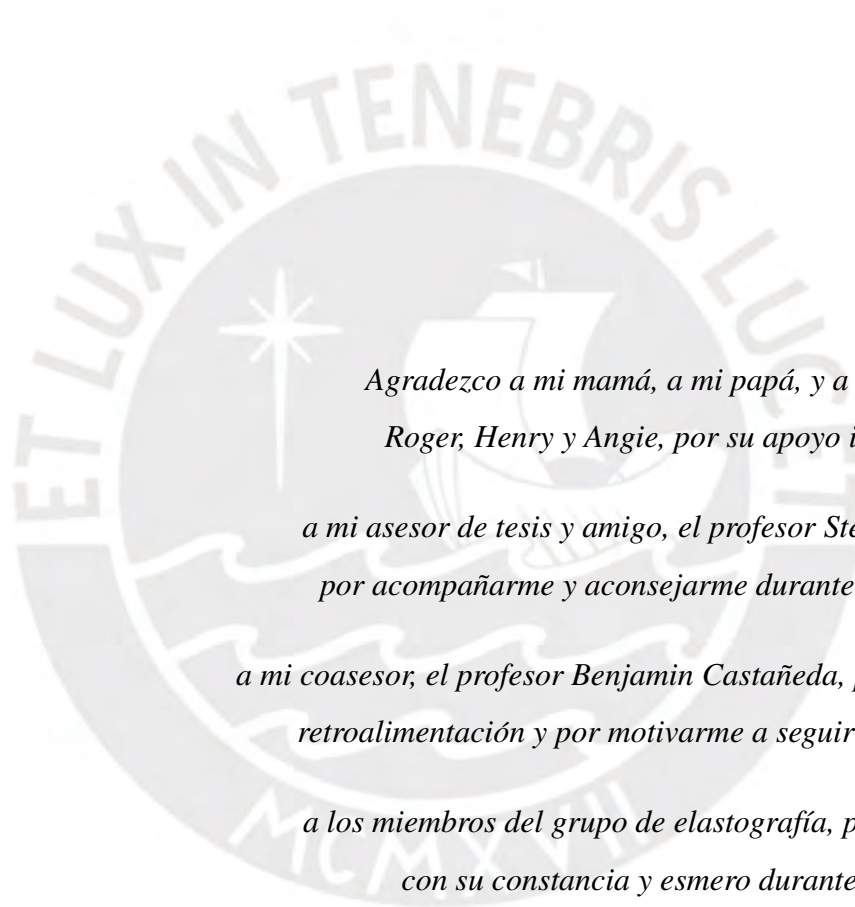
elevadas. Se demostró que los algoritmos propuestos no necesitan todo el vídeo de sonoelastografía para generar un mapa de velocidad de la onda de corte, sino un solo fotograma. Esto permite la visualización en tiempo real de la velocidad de la onda de corte, lo que puede beneficiar a diversas aplicaciones clínicas.



Abstract

Ultrasound elastography is a noninvasive imaging technique that aims to provide information about the elasticity of biological tissues by evaluating their biomechanical properties. It provides valuable information about their stiffness, which is related to biomechanical changes caused by pathological conditions. This makes it a valuable tool for diagnosing and monitoring the treatment of diseases such as cancer. One of the quantitative elastography methods is based on the use of two vibration sources to generate an interference pattern in the tissue. The shear wave can be visualized in real time by sonoelastography and an inversion scheme must be applied to recover the shear wave velocity from several frames. However, estimators studied in the literature exhibit some limitations such as poor performance in noisy environments, and long acquisition and processing times for real-time applications.

In this thesis, two algorithms, based on the Short-Time Fourier Transform and the Continuous Wavelet Transform, are proposed and implemented for shear wave velocity estimation. Homogeneous and heterogeneous gelatin phantoms were fabricated to evaluate the performance of the algorithms under controlled conditions. Sonoelastography experiments were performed at different vibration frequencies to evaluate their accuracy in a range of scenarios. The results show that the developed algorithms are comparable to existing estimators in terms of bias, coefficient of variation, contrast-to-noise ratio and resolution. In homogeneous media, the coefficient of variation remained below 10% for both estimators and, in heterogeneous media, the Continuous Wavelet Transform achieved a contrast-to-noise ratio of 30 dB on average. In general, the algorithms show superior robustness, especially in the presence of poor signal-to-noise ratio and in stiffer tissues with higher shear wave velocities. It was shown that the proposed algorithms do not need the entire sonoelastography video to generate a shear wave velocity map, but only a single frame. This allows real-time visualization of the shear wave velocity, which can benefit various clinical applications.



*Agradezco a mi mamá, a mi papá, y a mis hermanos
Roger, Henry y Angie, por su apoyo incondicional;
a mi asesor de tesis y amigo, el profesor Stefano Romero,
por acompañarme y aconsejarme durante esta travesía;
a mi coasesor, el profesor Benjamin Castañeda, por su valiosa
retroalimentación y por motivarme a seguir investigando;
a los miembros del grupo de elastografía, por inspirarme
con su constancia y esmero durante la pandemia;
a Esfano Machado, por animarme a entrar al mundo de la investigación;
y a Mabel, por darme su apoyo en momentos donde me sentía desmotivado.*



*Ir y venir, seguir y guiar, dar y tener,
entrar y salir de fase.
Amar la trama más que el desenlace.*

Jorge Drexler

Index

1	Problem framework	1
1.1	Ultrasound elastography: basic concepts	1
1.1.1	Ultrasound imaging	1
1.1.2	Elastography	2
1.1.3	Crawling Waves Sonoelastography	4
1.2	State of the art	5
1.2.1	Local frequency estimator	5
1.2.2	Auto-correlation	6
1.2.3	Phase Derivative (PD)	6
1.2.4	WAVE and R-WAVE	6
1.3	Justification	7
1.4	Objectives	7
1.4.1	General	7
1.4.2	Specific	7
2	Theoretical Background	8
2.1	Sonoelastography	8
2.1.1	Doppler Imaging	8
2.1.2	Vibration amplitude estimation	10
2.2	Shear wave propagation	12
2.2.1	Wave propagation in elastic media	12
2.2.2	Shear wave interference pattern	13
2.3	SWS estimation	14
2.3.1	Phase Derivative	14

2.3.2	R-WAVE	15
2.4	Time-Frequency analysis	16
2.4.1	Short-Time Fourier Transform	16
2.4.2	Continuous Wavelet Transform	17
3	Materials and Methods	18
3.1	Estimation algorithms	18
3.1.1	Algorithm for the STFT	18
3.1.2	Algorithm for CWT	20
3.1.2.1	Wavelet Ridges	20
3.1.2.2	Choice of wavelet and wavelet hyperparameters	20
3.2	Data acquisition	22
3.2.1	Materials	22
3.2.2	Equipment and protocol	23
3.2.3	Pre-processing	24
3.3	Metrics	25
4	Results	29
4.1	Homogeneous phantoms	29
4.2	Heterogeneous phantoms	33
4.3	SWS from a single frame	38
4.4	Discussion	38
	Conclusions	41
	Recommendations	42
	Bibliography	43

Figure index

1.1	B-mode image generation	2
1.2	Colour flow imaging modes. (a) Color Doppler image of an artery showing the direction of blood flow. (b) Power Doppler image of the same artery [1].	3
1.3	Crawling Waves Sonoelastography experiment [2]. (a) Experimental setup when imaging a gelatin phantom. One vibration source is attached to each side. (b) Power Doppler frame. (c) Generated SWS map	4
2.1	Process of obtaining a Doppler signal. (a) Moving target for 4 consecutive pulses. (b) Received echoes. (c) Doppler signal, which is composed of the echo amplitude for each pulse [1].	9
2.2	Block diagram of the framework of estimating the SWS via PD [3]	15
2.3	Wavelength measurement in interference pattern along a certain depth. The peak-to-peak distance is equal to half a wavelength.	15
3.1	(a) Sonoelasticity video frame at 360 Hz. The transform is computed across the lateral dimension for each depth. (b) CWT magnitude scalogram for 18 mm depth. The maximum amplitudes of the transform for each x coordinate are calculated and marked as a black line.	21
3.2	Scaled Morse wavelet with $P_{\beta,\gamma}^2 = \pi$, $\gamma = 3$ and central frequency $f_c = 287.6$ m ⁻¹	22
3.3	Pictures from the preparation procedure of the gelatin phantoms. The picture from the left shows a mix with 15% gelatin concentration, which is poured in the gap from the gelatin in the right picture.	23
3.4	Flow diagram of the data acquisition process to obtain the B-mode images and the sonoelastography videos	24

3.5	Sonoelastography pictures before and after applying the median filter and depth normalization. Images were generated with a vibration frequency of 350 Hz.	25
3.6	Directional filter on the frequency domain. The right image only includes two quadrants to enhance waves moving from right to left.	26
3.7	Effect of the directional filter in a sonoelastography signal generated at 350 Hz.	26
3.8	Regions of interest (ROI) on top of the B-mode ultrasound image for the homogeneous and heterogeneous phantoms.	27
3.9	Averaged lateral profile of SWS measurements using PD and a sigmoid fit.	28
4.1	SWS maps on top of the B-mode ultrasound image obtained with a vibration frequency of 400 Hz. The left, middle, and right columns show the results for the phantoms with an 8%, 12%, and 20% gelatin concentration, respectively.	29
4.2	Mean SWS for each gelatin concentration. The limits for the vertical bars are given by the mean plus or minus the standard deviation.	30
4.3	CV for all frequencies in the three manufactured gelatin phantoms, shown as a percentage	31
4.4	SWS maps overlaid on top of B-mode images for each method from sonoelastography data obtained at a vibration frequency of 340 Hz.	33
4.5	Mean SWS and standard deviation at several frequencies from the assessed SWS estimators. The dotted lines indicate the ground-truth SWS.	34
4.6	CV for all frequencies in the inclusion and the background of the heterogeneous phantom, shown as a percentage	35
4.7	Bias for all frequencies in the inclusion and the background of the heterogeneous phantom, shown as a percentage	35
4.8	CNR and resolution for all frequencies of the heterogeneous phantom	36
4.9	SWS maps on top of the B-mode ultrasound image obtained with a vibration frequency of 400 Hz from a single sonoelastography frame and no directional filtering. The left, middle, and right columns show the results for the phantoms with an 8%, 12%, and 20% gelatin concentration, respectively.	38
4.10	Mean SWS for each gelatin concentration. The limits for the vertical bars are given by the mean plus or minus the standard deviation.	39

Table index

1.1	Applications of Crawling Waves Sonoelastography	5
3.1	Amount of each ingredient used for the elaboration of gelatin phantoms. L is the volume in liters of water and x is the concentration in	22
4.1	Results for PD in homogeneous phantoms	31
4.2	Results for R-WAVE in homogeneous phantoms	32
4.3	Results for the STFT in homogeneous phantoms	32
4.4	Results for the CWT in homogeneous phantoms	32
4.5	Results for PD in heterogeneous phantom	36
4.6	Results for R-WAVE in heterogeneous phantom	37
4.7	Results for the STFT in heterogeneous phantom	37
4.8	Results for the CWT in heterogeneous phantom	37

Chapter 1

Problem framework

The first chapter presents the problem of estimating the shear wave speed when Crawling Waves Sonoelastography is used. First, it explains the basic concepts surrounding ultrasound elastography, its applications and the description of the Crawling Waves Sonoelastography approach. Then, some developed estimators are outlined, along with their limitations. Finally, the justification and objectives of the thesis are laid out.

1.1 Ultrasound elastography: basic concepts

1.1.1 Ultrasound imaging

Ultrasound has emerged as a widely utilized medical imaging modality, primarily attributable to its immediate results, absence of radiation exposure, and cost-effectiveness in comparison to alternative methods. It is based on the pulse-echo principle, illustrated in Figure 1.1.

A short-duration pressure wave, in the order of MHz, is transmitted through the tissue. This is achieved with an ultrasound transducer composed of piezoelectric elements that convert electrical signals into mechanical movements [1]. Echoes are generated according to the acoustic properties and geometry of the tissue and are received with the same transducer. Given that the speed of sound is approximately constant in most biological tissues, the signals can be processed to match the echoes with the locations where they were generated. Subsequently, an image that shows the geometry of the tissue can be generated. In B-mode imaging, the brightness of each pixel of the image is related to the strength or amplitude of the

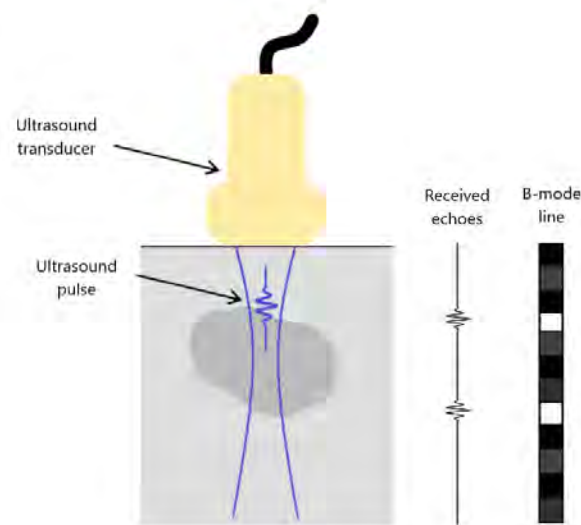


Figure 1.1: B-mode image generation

echo [4].

Many clinically implemented ultrasound systems also have modalities that aim to detect and quantify motion, which are known as “Doppler ultrasound” [1]. They achieve this by sending a set of ultrasound pulses at a certain Pulse Repetition Frequency (PRF) and analyzing the received signal. When a two-dimensional velocity image is generated, this mode is denominated Color Flow Imaging. This feature is typically used to image blood flow in arteries, veins, and the heart, although it can also detect tissue motion in general. In most scanners, two kinds of images can be generated: Color Doppler and Power Doppler. These are usually superimposed on the B-mode image, as shown in Figure 1.2. In the first one, the direction of the flow is color-coded, in a scale that typically goes from blue to red, where blue indicates a flow coming towards the transducer and red indicates a flow moving away from it. In the latter, the power of the Doppler signal is displayed, which is related to the intensity of flow.

1.1.2 Elastography

Elastography encompasses a group of techniques that aim to extract and quantify the mechanical properties of tissue. Many pathologies can alter these properties, making it a useful tool for diagnosis. For instance, liver diseases usually alter liver stiffness, so elastography can be used to determine the stage of fibrosis [5]. By providing a non-invasive

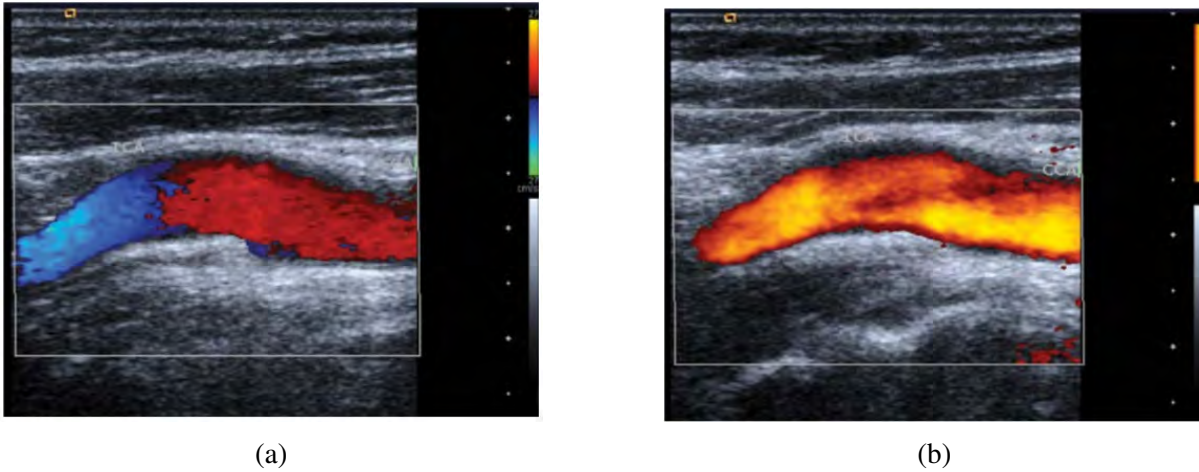


Figure 1.2: Colour flow imaging modes. (a) Color Doppler image of an artery showing the direction of blood flow. (b) Power Doppler image of the same artery [1].

method to evaluate these conditions, clinicians can stage liver disease with greater precision, monitor the progression of fibrosis, and gauge the effectiveness of treatments over time, all without resorting to invasive liver biopsies. Elastography can also be used in breast cancer screening [6], where it helps distinguish between benign and malignant formations, and in tendinopathy, where it can even detect some pathological changes before they are visible in conventional ultrasound imaging [7].

There are several methods available for elastography, which may differ in what they measure and how they measure it. In general, they can be classified into quasi-static, harmonic, or transient methods [8, 9]. In quasi-static methods, a compression force is applied to the tissue, and the local strain is measured based on how much the tissue is displaced. This is often used as a qualitative technique because the strain of the structure under analysis is compared to the strain of the adjacent tissues [1]. In contrast, both harmonic and transient methods typically attempt to estimate Shear Wave Speed (SWS) as another method for quantifying tissue stiffness. Shear waves are waves whose direction of propagation is perpendicular to the particle displacement, contrary to pressure waves, in which the direction of propagation is the same as the direction of the displacement. In the human body, the speed of propagation of shear waves (1 to 10 m/s [9]) is two or three orders of magnitude lower than the speed of pressure waves (around 1500 m/s [1]). As a consequence, ultrasound systems can use pressure waves to generate B-mode images and to track the shear wave propagation. In harmonic methods, one or several vibration sources can be utilized to excite tissue at a low

frequency (from 10Hz to 10kHz) and generate the shear waves. Lastly, in transient methods, a short-duration wave is generated and the tissue response is monitored to estimate SWS. This can be done with either an external actuator or with the transducer itself, using what is known as acoustic radiation force (ARF) [1].

1.1.3 Crawling Waves Sonoelastography

Crawling Waves Sonoelastography is a harmonic elastography technique that uses two vibration sources to generate an interference pattern in tissue. For context, most elastography methods that aim to quantify shear velocity rely on frame rates greater than 1 kHz to accurately track the shear wave propagation. Although this is achievable nowadays with ultrafast imaging [10], most scanners used in typical clinical settings have lower frame rates for Doppler Imaging [8]. For that reason, Wu et al. [11] developed a method that enabled the tracking of the shear wave propagation in real-time. It is based on sonoelastography, which estimates the vibration amplitude of a certain region using the Doppler mode [12]. By using vibration sources with slightly different frequencies, a moving interference pattern can be generated. Its apparent velocity is proportional to the true SWS and can be estimated from the sonoelastography video. This process is illustrated in Figure 1.3.

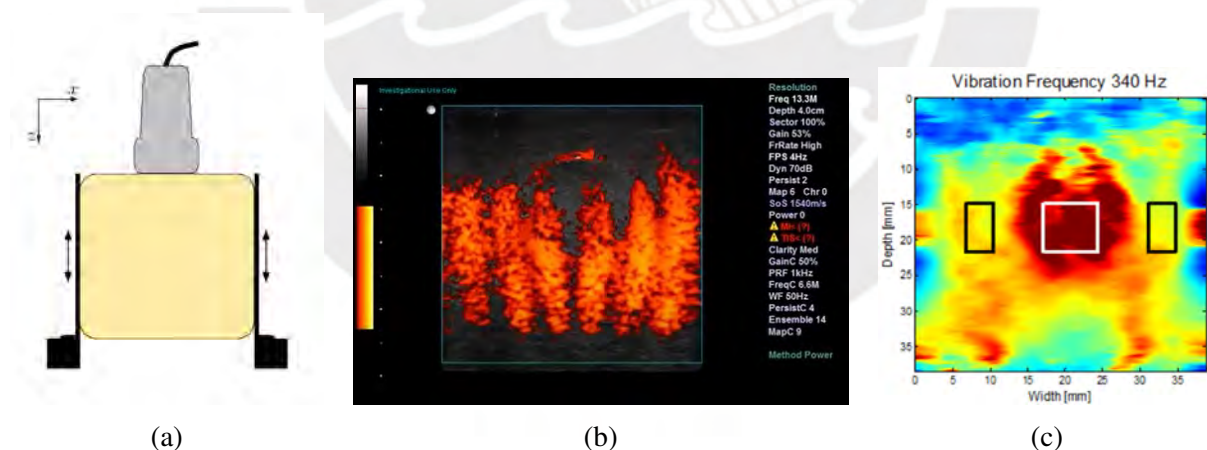


Figure 1.3: Crawling Waves Sonoelastography experiment [2]. (a) Experimental setup when imaging a gelatin phantom. One vibration source is attached to each side. (b) Power Doppler frame. (c) Generated SWS map

The feasibility of the method has been tested for both diagnosis and tissue characterization, as shown in table 1.1. The proposed technique also brings some advantages when compared

to other elastography methods. To begin with, as most of the energy in the crawling waves is aligned in the axial direction, higher penetration depths can be achieved. In addition, the crawling waves can be visualized in real time by conventional Doppler imaging scanners at typical Doppler frame rates, which facilitates data acquisition. Lastly, because the local shear wave velocity can be estimated from the local shear wavelength, numerous inversion schemes can be utilized.

Modality	Organ	Function
Ex vivo	Thyroid	Detection of thyroid nodules [13]
	Prostate	Prostate cancer diagnosis [14]
	Liver	Hepatic Steatosis diagnosis [15]
In vivo	Skin	Dermis characterization [16]
	Muscle	Muscle characterization [3]

Table 1.1: Applications of Crawling Waves Sonoelastography

This thesis aims to tackle the inversion problem of recovering a SWS map from a sonoelastography video, which shows the shear wave propagation. Several studies have attempted to address this issue, and these will be outlined in the following section.

1.2 State of the art

Many algorithms have been developed for SWS estimation. An outline of the most relevant methods used in Crawling Waves Sonoelastography is presented in the following section.

1.2.1 Local frequency estimator

When the method was first implemented in heterogeneous media [17], i.e. phantoms with inclusions, a local frequency estimator based on log-normal quadrature filters was used [18, 19]. This allowed the computation of a SWS map from a single sonoelastography frame. However, one disadvantage of this approach is that it requires amplitude normalization and trend removal to avoid spectral leakage artifacts [20].

1.2.2 Auto-correlation

Another approach proposed in [20] uses a 1D kernel window, which is translated across a region of interest to estimate the local shear velocity from the auto-correlation. This method was also adapted to use a 2D kernel, incorporating both the axial and lateral dimensions, which resulted in improved accuracy and less noise. Additionally, there is a trade-off between accuracy and spatial resolution when varying the kernel size. The method was tested in heterogeneous phantoms and *ex vivo* livers [21].

1.2.3 Phase Derivative (PD)

The shear velocity can also be estimated by estimating the local wave number, which is equal to the phase derivative. Estimation of the phase, as proposed in [22], can be done pixel by pixel by taking the Fourier Transform across the slow-time domain. This is usually a noisy estimate, thus some smoothing is required to avoid the amplification of error when taking the derivative. The method, also denoted as PD, was tested in heterogeneous phantoms, excised mouse livers, and *in vivo* muscle tissue [3].

1.2.4 WAVE and R-WAVE

Wavelength Average Velocity Estimator (WAVE) consists of measuring the wavelengths and averaging them across the time domain [23]. It allows fast computation of the SWS, but estimates can be inaccurate, and a directional filter is required to achieve the desirable results. On the other hand, a regularized version of this algorithm, denominated R-WAVE, was also developed [24]. It used the phase information to create an over-determined linear system and applied Tikhonov regularization to estimate shear velocity. The performance of this method has been compared to previously proposed estimators, including the approaches based on the autocorrelation and PD, mentioned earlier. In heterogeneous gelatin phantoms, it has been found to reduce estimation errors and improve the contrast-to-noise ratio by 5 dB. However, it also presents a higher execution time.

1.3 Justification

Despite its advantages, Crawling Waves Sonoelastography still has certain limitations. One of them is that many of the developed estimators do not have optimal performance in noisy environments. Given the importance of reliability and accuracy in clinical applications, there is a constant pursuit of a robust algorithm to ensure reproducible results.

In addition, most of the estimators in the state of the art require the total length of the recording to obtain a single SWS map, preventing real-time visualization. If possible, this would provide valuable feedback to the operator during the acquisition process, facilitating immediate assessment and potentially improving the overall effectiveness and efficiency of the method.

1.4 Objectives

1.4.1 General

Develop and implement two novel algorithms for SWS estimation based on space-frequency decomposition within the framework of Crawling Waves Sonoelastography and validate their performance in homogeneous and heterogeneous gelatin phantoms.

1.4.2 Specific

- Implement two algorithms based on the Short-Time Fourier Transform and the Continuous Wavelet Transform in Matlab.
- Generate SWS maps from gelatin homogeneous and heterogeneous phantoms using the developed algorithms.
- Conduct a comparative analysis between the algorithms and existing SWS estimators in terms of bias, coefficient of variation, contrast-to-noise ratio, and resolution.

The results of this thesis have been presented at two conferences and published in the conference proceedings [25, 26].

Chapter 2

Theoretical Background

2.1 Sonoelastography

Sonoelastography imaging has been around for more than thirty years [8]. The following section aims to thoroughly explain how a sonoelastography signal is generated, how it is processed to measure vibration amplitude, and the problems that can arise when it is computed.

2.1.1 Doppler Imaging

Doppler imaging was initially developed to measure blood flow velocity and visualize the flow in the body. Two techniques can be applied to measure velocity: Continuous-wave Doppler and Pulse-wave Doppler. The former is based on the Doppler effect, which explains the frequency shift when a wave source moves relative to an observer. The latter, which is the most widely used, is based on sending many ultrasound pulses and analyzing their echoes. Below, the principles of Pulsed-Wave Doppler will be described, including the two main imaging modalities: Color and Power Doppler.

An ultrasound pulse $p(t)$ is sent at a certain Pulse Repetition Interval (PRI). An ensemble of N samples is considered to calculate velocity. Considering a scatterer located at a distance d from the transducer, according to the pulse-echo principle, the received signal is shown in

Equation 2.1.

$$\begin{aligned}
 s(t) &= p\left(t - \frac{2d}{c}\right) + p\left(t - \frac{2d}{c} - PRI\right) + p\left(t - \frac{2d}{c} - 2PRI\right) + \dots \\
 &= \sum_{i=1}^N p\left(t - \frac{2d}{c} - iPRI\right).
 \end{aligned}
 \tag{2.1}$$

The velocity of sound in tissue c is considered to be 1540m/s [1]. If the scatterer is moving towards the transducer at a velocity v , then its distance from it would be $d = d_0 - vt$, where d_0 is its initial position. The resulting signal is shown in Equation 2.2.

$$s(t) = \sum_{i=1}^N p\left(t - iPRI - \frac{2}{c}(d_0 - vt)\right).
 \tag{2.2}$$

To obtain the velocity at the point located at d_0 , the signal is sampled at $t = \frac{2d_0}{c} + kPRI$, which means that one sample per pulse is taken. The result is known as the Doppler signal, expressed in Equation 2.3.

$$s[k] = p\left(\frac{2v}{c}\left(\frac{2d_0}{c} + kPRI\right)\right).
 \tag{2.3}$$

This process is illustrated in Figure 2.1.

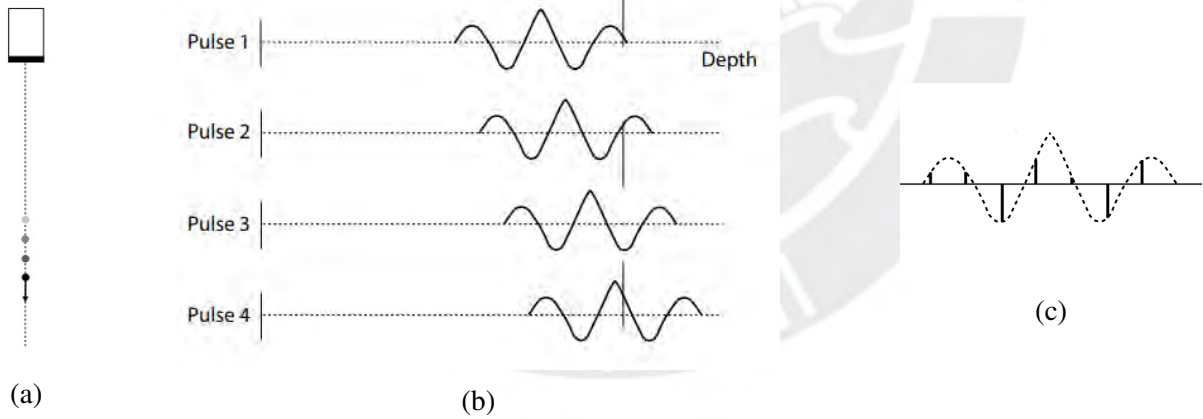


Figure 2.1: Process of obtaining a Doppler signal. (a) Moving target for 4 consecutive pulses. (b) Received echoes. (c) Doppler signal, which is composed of the echo amplitude for each pulse [1].

Additionally, the variable $\tau = kPRI$ is defined as the “slow-time”. The Doppler signal is equivalent to sampling a signal in the slow time domain at a certain frequency, which is known

as the pulse repetition frequency $PRF = 1/PRI$. The result is expressed in Equation

$$s(\tau) = p\left(\frac{2v}{c}\tau + \phi\right). \quad (2.4)$$

Considering $p(t)$ is a narrow-band signal with center frequency f_0 , the center frequency of a Doppler signal would be $f_D = \frac{2v}{c}f_0$. Additionally, the Nyquist theorem shows an upper bound for the maximum velocity that can be measured, which is expressed in Equation 2.5.

$$f_{D(max)} = \frac{PRF}{2} \implies v_{max} = PRF \frac{c}{4f_0}. \quad (2.5)$$

If a particle moves at a higher rate, aliasing can occur.

Following that, for the computation of particle velocity, the center frequency of the frequency spectrum needs to be found. However, computation of the whole spectrum is often computationally costly. For that reason, Kasai *et al* [27] derived a simple method to calculate mean frequency and spectral variance from the autocorrelation function of the Doppler signal $R[k]$ and its phase $\phi[k]$. This is displayed in Equations 2.6 and 2.7.

$$\bar{\omega} = \frac{\phi[1]}{PRI}, \quad (2.6)$$

$$\sigma^2 = \frac{2}{PRI^2} \left(1 - \left|\frac{R[1]}{R[0]}\right|\right). \quad (2.7)$$

The autocorrelation function is often derived from the packet of N pulses with Equation 2.8.

$$R[k] = \sum_{n=0}^{N-2} s[n+k]s^*[n]. \quad (2.8)$$

Lastly, an accurate estimation requires the elimination of echoes from stationary or slowly moving tissue, which is achieved by high-pass filtering. Typically, a filter characterized by a sharp response, commonly referred to as the ‘‘Wall Filter’’, is selected for this purpose [4].

2.1.2 Vibration amplitude estimation

Now a particle moving harmonically will be analyzed. A target vibrating with amplitude ϵ_v at a frequency ω_v has a variable depth of $d = d_0 - \epsilon_v \sin(\omega_v t)$. From Equation 2.4, the received

signal is derived in Equation 2.9.

$$s(\tau) \approx \exp \left(j\omega_0 \frac{2\epsilon_v}{c} \sin(\omega_v \tau + \phi) \right). \quad (2.9)$$

Consequently, the Jacobi-Anger expansion, widely used in FM signals analysis, can be used. The resulting signal is shown in 2.10.

$$s(\tau) \approx \sum_{n=-\infty}^{+\infty} J_n(\beta) e^{jn(\omega_v \tau + \phi)}, \quad (2.10)$$

where J_n is the Bessel function of the first kind of order n and $\beta = \frac{2\epsilon_v \omega_0}{c}$ is the modulation index.

This gives us an insight into what we can expect when a Doppler signal from a vibrating object is received. A vibrating object generates a frequency-modulated signal, whose modulation index is proportional to its vibration amplitude. In [12], a relationship between the modulation index β and the Doppler spectral spread is derived. Therefore, it can be concluded that the vibration amplitude of the signal is proportional to the standard deviation of the spectrum σ , according to the Equation 2.11.

$$\epsilon_m = \frac{c}{\sqrt{2\omega\omega_v}} \sigma. \quad (2.11)$$

The variance of the spectrum can be obtained from Equation 2.7, so an image of the vibration amplitude of the excited tissue can be generated. This is the main principle on which sonoelastography is based. However, there is a limit to vibration amplitude that can be measured. Because of the Nyquist frequency, the maximum frequency that can be measured when sampling the signal in Equation 2.10 is $PRF/2$. If the vibration amplitude is too high, some spectral components may extend beyond this limit, so aliasing can occur [28]. Furthermore, the use of a wall filter, which is common in Doppler imaging, can be detrimental to the obtained result. The effect of the chosen wall filter, PRF, and ensemble length is analyzed in [29].

2.2 Shear wave propagation

The next section explains the principles governing motion in elastic media and what occurs when using Crawling Waves Sonoelastography. This includes how a shear wave propagates, how it is related to the stiffness of the medium, and how the tissue responds when two vibration sources are used.

2.2.1 Wave propagation in elastic media

In an elastic solid, the conservation of linear momentum, accounting for external forces acting on the surface and internal body forces, can be written in integral form. This is shown in Equation 2.12, where ρ is the density, \mathbf{u} is the displacement vector, $\boldsymbol{\sigma}$ is the stress tensor, and \mathbf{f} is the body force per unit mass vector.

$$\frac{d}{dt} \iiint_V \rho \dot{\mathbf{u}} = \iint_S \boldsymbol{\sigma} d\mathbf{S} + \iiint_V \rho \mathbf{f} dV, \quad (2.12)$$

Using the divergence theorem, Equation 2.12 is rewritten in differential form in Equation 2.13.

$$\rho \ddot{\mathbf{u}} = \nabla \cdot \boldsymbol{\sigma} + \rho \mathbf{f}. \quad (2.13)$$

Considering that the effects of internal body forces are negligible, $\mathbf{f} \approx 0$. Then, the strain tensor can be expressed in terms of the strain using the linear relationship between strain and stress. Furthermore, for small deformations, the strain can be expressed in terms of derivatives of the displacement, so the same Equation can be obtained in terms of the displacement vector alone [30], as shown in Equation 2.14, where λ and μ are known as the first and second Lamé parameters.

$$(\lambda + \mu) \nabla (\nabla \cdot \mathbf{u}) + \mu \nabla^2 \mathbf{u} = \rho \ddot{\mathbf{u}}, \quad (2.14)$$

The Lamé parameters are related to Young's modulus E and Poisson's ratio ν by equations 2.15 and 2.16.

$$\lambda = \frac{E\nu}{(1+\nu)(1-2\nu)}, \quad (2.15)$$

$$\mu = \frac{E}{2(1+\nu)}. \quad (2.16)$$

Then, the displacement vector \mathbf{u} can be split into two by using the Helmholtz Equation, $\mathbf{u} = \mathbf{u}_c + \mathbf{u}_s$. The theorem states that any vector field can be decomposed into the sum of an irrotational field ($\nabla \times \mathbf{u}_c = 0$) and a solenoidal field ($\nabla \cdot \mathbf{u}_s = 0$). The irrotational field accounts for compressional waves, and the solenoidal field accounts for shear waves [8]. This implies that the displacements within an elastic can be decomposed into a pressure field and a shear wave field.

Considering only the shear displacement \mathbf{u}_s , the shear wave Equation can be derived from Equation 2.14 in Equation 2.17.

$$\nabla^2 \mathbf{u}_s = \frac{1}{c_s^2} \ddot{\mathbf{u}}_s. \quad (2.17)$$

The constant c_s , which corresponds to the SWS, is defined in Equation 2.18.

$$c_s = \sqrt{\frac{\mu}{\rho}} = \sqrt{\frac{2E}{(1+\nu)\rho}}. \quad (2.18)$$

When specifically analyzing biological tissues, a consideration that must be made is that they are nearly incompressible, meaning their Poisson ratio ν is approximately 0. Replacing $\nu = 0$ in Equation 2.18 gives $c_s = \sqrt{\frac{E}{\rho}}$, which links the SWS and the stiffness of the material [31]. Therefore, by imaging the SWS in tissue, we can detect regions with abnormal stiffness and quantify it.

2.2.2 Shear wave interference pattern

In Crawling Waves Sonoelastography, a shear wave interference pattern is generated by placing two vibration sources with slightly different frequencies at each side of the region of interest. When using parallel plates, the wave propagation is modeled as the superposition of two plane waves coming from each side in Equation 2.19, where u is the particle displacement, α is the attenuation coefficient, D is the distance between sources and k_i is the wave number that corresponds to the frequency ω_i .

$$\begin{aligned} u(x, t) &= u_{right} + u_{left}, \\ u(x, t) &= e^{-\alpha(D/2+x)} e^{-j(k_1(D/2+x)-\omega_1 t)} + e^{-\alpha(D/2-x)} e^{-j(k_2(D/2-x)-\omega_2 t)}. \end{aligned} \quad (2.19)$$

With sonoelastography, the vibration amplitude of a target is estimated, which corresponds to the envelope of the particle displacement. This can be derived from the relationship in Equation 2.20.

$$|u(x, t)|^2 = (u_{right} + u_{left})(u_{right} + u_{left})^*. \quad (2.20)$$

By replacing Equation 2.19 in 2.20, we get 2.21.

$$|u(x, t)|^2 = 2^{-\alpha D} [\cosh(2\alpha x) + \cos((2k + \Delta k)x + \Delta\omega t)]. \quad (2.21)$$

Considering low attenuation, the hyperbolic term becomes approximately constant [32], so it can be filtered out. Therefore, the ideal signal, normalized by amplitude, is expressed in Equation 2.22.

$$s(x, t) = \cos((2k + \Delta k)x + \Delta\omega t). \quad (2.22)$$

Following that, a relationship between the wave number of the received signal (k_r) and the SWS is derived in Equation 2.23.

$$k_r = 2k + \Delta k = \frac{2\omega + \Delta\omega}{c_s}. \quad (2.23)$$

This relationship can be generalized to heterogeneous media [17], so the local SWS can be calculated from the local shear wave number using Equation 2.24.

$$c_s(x) = \frac{2\omega + \Delta\omega}{k_r(x)}. \quad (2.24)$$

2.3 SWS estimation

In this section, the principles for some algorithms found in the literature for SWS estimation are described, as well as their limitations.

2.3.1 Phase Derivative

It can be noted that extracting the phase from the signal obtained in Equation 2.22 can give information about the shear wavelength, which varies in space, meaning $\theta'(x) = 2k + \Delta k$.

Using the fact that $c = \omega/k = \Delta\omega/\Delta k$, the SWS can be calculated with Equation 2.25.

$$c(x) = \frac{2\omega + \Delta\omega}{\theta'(x)}. \quad (2.25)$$

Estimation of the phase can be done pixel by pixel through a slow-time filter [22]. In [3], a framework is proposed for fast computation of the algorithm. Firstly, the FFT across the slow-time is calculated and the phase corresponding to $\Delta\omega$ is extracted. Then, given that the phase is in the interval of $]-\pi, \pi]$, it needs to be transformed to a continuous signal, in a process known as phase unwrapping. Lastly, some additional smoothing is applied to the unwrapped phase to avoid amplifying errors when taking the derivative numerically [33]. This process is shown in Figure 2.2.

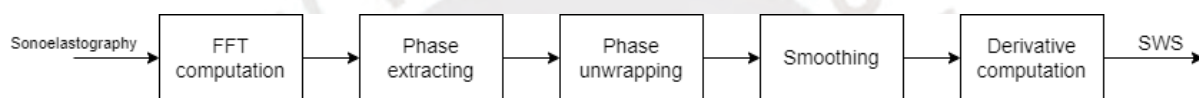


Figure 2.2: Block diagram of the framework of estimating the SWS via PD [3]

2.3.2 R-WAVE

This algorithm is based on a previous method. It uses a peak detection algorithm to measure wavelength. Due to noise, before direct measurement, a directional motion filter [34] is implemented in each depth slice. This is a band-pass 2D filter centered at $\Delta\omega$ with a spatial frequency range defined by an upper and lower limit for SWS (1-10 m/s). After measurement, the SWS is computed with the wavelength and is assumed to be equal to a weighted average of the local measurements between peaks, as shown in Figure 2.3 Each x_i represents local SWS

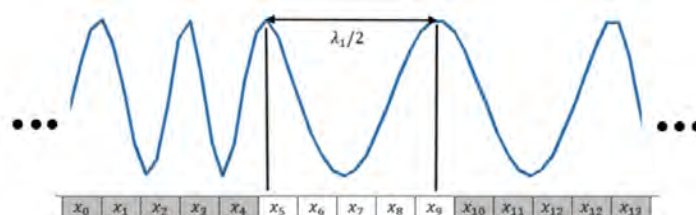


Figure 2.3: Wavelength measurement in interference pattern along a certain depth. The peak-to-peak distance is equal to half a wavelength.

and corresponds to a weighted coefficient a_j . For each measured wavelength, Equation 2.26 must hold.

$$a_5x_5 + a_6x_6 + a_7x_7 + a_8x_8 + a_9x_9 = \frac{1}{2}\lambda_1f = S_{av1} \quad (2.26)$$

The weighted coefficients are obtained from the phase estimate, which is computed from the Hilbert transform of the signal [24]. By repeating the process for each frame at the same depth, a system of equations of the form $Ax_j = S_{av}$ can be formed, where Ax_j is the weighted coefficient map and S_{av} is the measured average speed. Once computed, the result is an overdetermined linear system, which is solved with an iterative algorithm based on Tikhonov regularization. This algorithm finds the solution to Equation 2.27, where Γ is the Tikhonov matrix and α is the regularization coefficient.

$$\hat{x}_j = \operatorname{argmin} \left\{ \|Ax_j - S_{av}\|^2 + \alpha^2 \sum_{n=1}^N (|\Gamma x_j)_i|^2 + \beta)^{\frac{k}{2}} \right\}, \quad (2.27)$$

2.4 Time-Frequency analysis

In the final section of this chapter, two transforms are introduced to decompose a signal into a time-frequency representation. These are the basis of the algorithms described in the third chapter for estimating shear velocity.

2.4.1 Short-Time Fourier Transform

Time-frequency decomposition has been known for a long time. By using a short-duration window $w(t)$, a local frequency spectrum of a signal $x(t)$ can be computed from Equation 2.28.

$$X(\tau, \omega) = \int_{-\infty}^{+\infty} w(t - \tau)x(t)e^{j\omega t}dt. \quad (2.28)$$

This is known as the Short-Time Fourier Transform or STFT [35]. A discrete-time version of the transform is also well-known [36] and is expressed in Equation 2.29.

$$X(m, \omega) = \sum_{n=-\infty}^{+\infty} x[n]w[n - m]e^{-i\omega n}. \quad (2.29)$$

The STFT is often used to analyze non-stationary signals or to compute the periodogram

of a random process. It is important to mention that when analyzing any signal with this transform, there exists an inherent trade-off between frequency and spatial resolution, which can be controlled by adjusting the window size. The longer the window, the better frequency resolution and worse spatial resolution are obtained. The opposite is also true.

2.4.2 Continuous Wavelet Transform

A more modern approach to time-frequency decomposition is based on wavelets. Wavelets are a class of basis functions that have to fulfill certain requisites: they need to have zero-mean and square norm one. In other words, they need to have band-pass characteristics [37].

In continuous time, the Continuous Wavelet Transform or CWT of a signal $x(t)$ is obtained by computing the inner product of the signal with a wavelet, as Equation 2.30 shows.

$$W(\tau, s) = \frac{1}{s} \int_{-\infty}^{+\infty} x(t) \psi^* \left(\frac{t - \tau}{s} \right) dt. \quad (2.30)$$

The wavelet $\psi_{s,\tau}(t)$ is a scaled and translated version of another function called the mother wavelet, defined in Equation 2.31.

$$\psi_{s,\tau}(t) = \frac{1}{s} \psi \left(\frac{t - \tau}{s} \right). \quad (2.31)$$

The factor $1/s$ assures that the output of the CWT has the same amplitude as the signal [38]. For this reason, the transform can be interpreted as a filtering operation, in which the signal is convoluted with the time-reversed version of the wavelet. This is expressed in Equation 2.32.

$$W(\tau, s) = x(t) * \psi_s(-t). \quad (2.32)$$

In that sense, the CWT allows the decomposition of the signal into different frequency bands. For instance, if a wavelet has a peak frequency of f and a bandwidth B , the scaled wavelet $\psi_s(t)$ will have a peak frequency of sf and a bandwidth sB . The bands at lower frequencies have a better frequency resolution and a poor time resolution, while the bands at higher frequencies have a better time resolution and a poor frequency resolution [39]. This is an advantage compared to the STFT, which has a fixed resolution for all frequencies which depends on the window length.

Chapter 3

Materials and Methods

This chapter describes the proposed algorithms, the methodology used to perform the experiments, and the metrics to compare the results with the state-of-the-art. The first section describes the SWS estimation algorithms from the STFT and the CWT, as well as the election of hyperparameters such as the window length or wavelet. The next section discusses the data acquisition process, which includes the preparation of the gelatin phantoms, the setup to generate the vibration pattern, the equipment to acquire the ultrasound signal, and some pre-processing steps. Finally, the last section describes the metrics that will be used in the next chapter to quantify the performance of the proposed algorithms.

3.1 Estimation algorithms

3.1.1 Algorithm for the STFT

From the filtered version of the ideal sonoelastography signal, shown in Equation 2.22, a discrete version is derived in 3.1, where T_{lat} is the lateral separation between samples (also known as pitch) and ϕ is a phase that varies depending on time.

$$s[n] = A \cos(k_s n T_{lat} + \phi). \quad (3.1)$$

For the algorithm, the STFT is computed along the lateral dimension of the measured signal with maximum overlap. This is expressed in Equation 3.2, where $w[n]$ denotes the window and

L denotes its length in samples.

$$S(m, \omega) = \sum_{n=0}^L s[n]w[n - m]e^{-i\omega n}. \quad (3.2)$$

Ideally, the amplitude of the transform would be maximum in regions where the frequency ω is equal to the local shear wavelength of the signal k_s . As a consequence, a rough estimate of the shear wavelength can be obtained by finding the frequency that maximizes the transform's amplitude, which is expressed mathematically in Equation 3.3.

$$\hat{k}_s[m] = \arg \max_{\omega} |S(m, \omega)|. \quad (3.3)$$

Then, local SWS can be found using the relation $\hat{c}_s = (2\omega + \Delta\omega) / \hat{k}_s$, derived in the previous chapter.

The window and window size must be selected carefully to achieve the expected results. In this application, prioritizing the spatial resolution is crucial to accurately distinguish the boundaries between regions with contrasting SWS. Frequency resolution, on the other hand, holds less significance as the signal is composed of a single varying frequency component. Consequently, a smaller window size is selected. Nonetheless, it is important to note that the window size cannot be arbitrarily reduced; therefore, the window length is determined so that at least a wavelength of the signal is included. To do this, an upper bound for SWS must be considered, which results in a minimum wave number (Equation 3.4) from which the window size can be determined (Equation 3.5).

$$k_{min} = \frac{2\omega + \Delta\omega}{c_{max}} \quad (3.4)$$

$$L = \left\lceil \frac{2\pi}{k_{min}} \frac{1}{T_{lat}} \right\rceil \quad (3.5)$$

In addition, a Hamming window function is chosen for $w[n]$ to avoid spectral leakage artifacts.

Given that the algorithms are applied to a one-dimensional signal, the calculation is repeated for each depth step and for each frame of the sonoelastography video. This results in a SWS video, which should have the same measurements across all time samples.

3.1.2 Algorithm for CWT

3.1.2.1 Wavelet Ridges

Like the STFT, the CWT offers a means to analyze a signal across space and frequency. Each scale corresponds to a scaled version of the mother wavelet, which has a central frequency k_{peak} . Considering this, a similar procedure to the one described in the previous section can be followed. Firstly, a filter bank is generated from the chosen wavelet and the discretized scales. For the discretization of the scales, an upper and lower bound for SWS must be selected. This range is based on the usual velocities found in biomaterials, which go from 2 to 10 m/s approximately [40]. Following that, a shear wave number range can be obtained, where the lower and upper bound can be calculated from Equation 3.4. For the step size, 48 scales per octave were considered, as it provided sufficient resolution for the estimated SWS. This means that the scale doubles every 48 steps: $s = 2^{i/48}$. Then, the transform is computed with Equation 3.6.

$$W(m, s) = s[n] * \psi_s[-n]. \quad (3.6)$$

Subsequently, the local shear wavelength can be estimated with Equation 3.7.

$$\hat{k}_s[m] = k_{peak} \times \arg \max_s |W(m, s)| \quad (3.7)$$

These points, in which the scale corresponds to a local maximum of the transform, are also known as amplitude ridge points [41]. Once a local shear wavelength is found, the SWS can be found using the relation $\hat{c}_s = (2\omega + \Delta\omega) / \hat{k}_s$. An illustration of the algorithm is shown in figure 3.1. For implementation, the Wavelet Toolbox from Matlab [42] is used.

As with the STFT, the calculation is repeated for each depth step and for each frame of the sonoelastography video.

3.1.2.2 Choice of wavelet and wavelet hyperparameters

The generalized Morse Wavelet was selected because of its flexibility, with two adjustable hyperparameters, allowing customization for this specific application. It is defined in the continuous frequency domain with Equation 3.8, where $u(\omega)$ is the unit step function, α is a

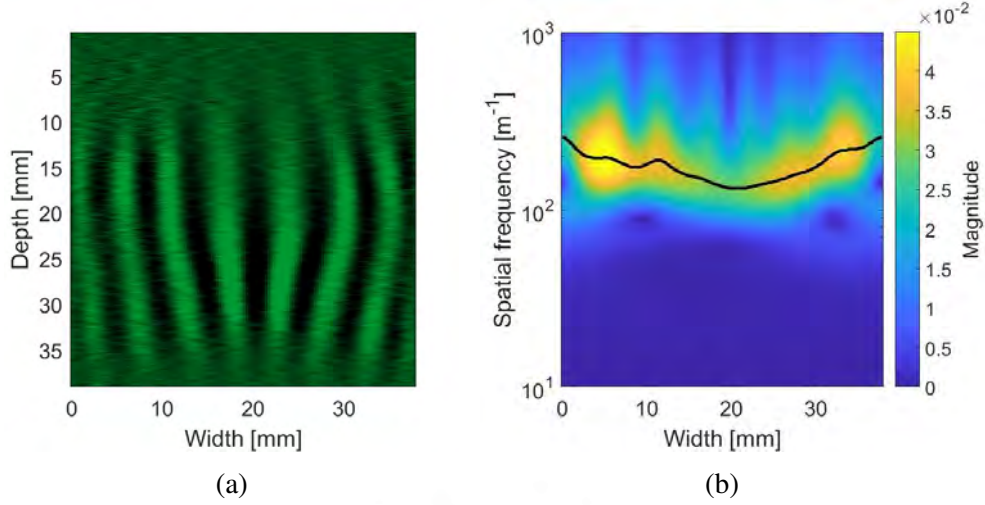


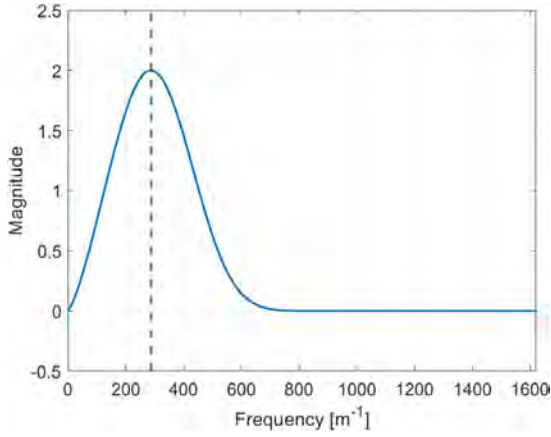
Figure 3.1: (a) Sonoelasticity video frame at 360 Hz. The transform is computed across the lateral dimension for each depth. (b) CWT magnitude scalogram for 18 mm depth. The maximum amplitudes of the transform for each x coordinate are calculated and marked as a black line.

normalization constant, and β and γ control the wavelet shape.

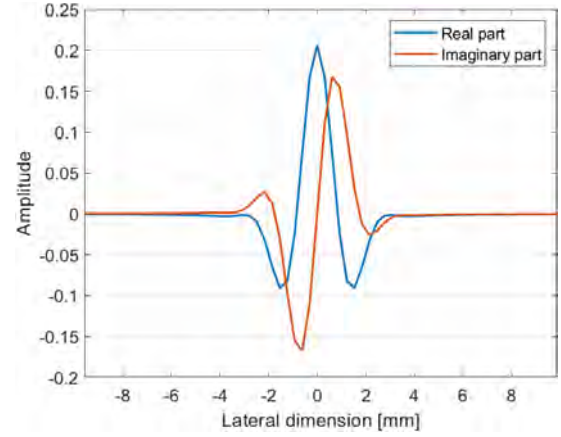
$$\Psi(\omega) = \alpha u(\omega) e^{-\omega^\gamma} \omega^\beta. \quad (3.8)$$

This is an analytic wavelet, meaning its spectrum has only positive frequencies ($\Psi(\omega) = 0 \quad \forall \omega < 0$). Analytic wavelets allow recovery of the instantaneous amplitude and phase of the input signal [41]. Besides that, the central frequency of the Morse Wavelet is $\omega_{\beta,\gamma} = (\beta/\gamma)^{(1/\gamma)}$. This value is utilized to calculate shear wavelength.

Another parameter of interest is the time-bandwidth product $P_{\beta,\gamma} = \sqrt{\beta\gamma}$. It can be interpreted as the wavelet's duration, since $P_{\beta,\gamma}/\pi$ is the number of oscillations that fit in the central window of the wavelet in the time domain [43]. Subsequently, to enhance spatial resolution, a time-bandwidth product of π is selected, so that at least the wavelet includes one oscillation within its duration. For the Gamma parameter, it is shown that setting $\gamma = 3$ closely resembles a Gaussian window in the frequency domain [43], so this value is also selected. An illustration of the wavelet with the selected parameters, considering the sampling frequency in the spatial domain, is found in Figure 3.2.



(a) Wavelet in the frequency domain



(b) Wavelet in the spatial domain

Figure 3.2: Scaled Morse wavelet with $P_{\beta,\gamma}^2 = \pi$, $\gamma = 3$ and central frequency $f_c = 287.6 \text{ m}^{-1}$

3.2 Data acquisition

3.2.1 Materials

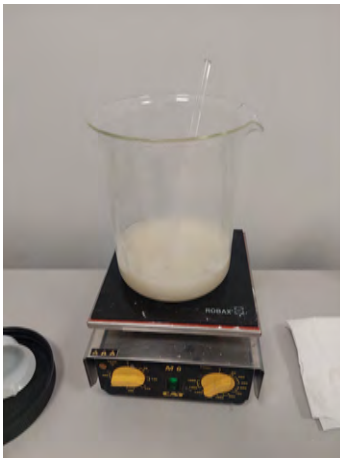
A set of gelatin phantoms was elaborated for testing, using a mixture of water, gelatin powder, corn starch, salt, and agar, following the framework in [3]. The specific quantity of each ingredient in grams is provided in Table 3.1, which depends on the volume of water L in liters and the gelatin concentration x .

Material	Mass [g]
Gelatin	$Lx/(1-x)$
Corn starch	$0.02L$
Salt	$0.009L$
Agar	$0.0015L$

Table 3.1: Amount of each ingredient used for the elaboration of gelatin phantoms. L is the volume in liters of water and x is the concentration in

The gelatin concentration is normally expressed as a percentage, and it is approximately proportional to the hardness of the gelatin, so a higher concentration results in a higher SWS. The homogeneous phantoms were prepared using three different mixtures containing gelatin concentrations of 8%, 12%, and 20%. These values were selected so the SWS of the phantoms ranged from 2 to 9 m/s [29, 44], as these are the typical values in tissue [8]. To achieve homogeneity, the compounds were heated to 100°C and thoroughly mixed. Subsequently, they were allowed to cool down for an hour in a plastic container measuring 15 cm in width, 10 cm

in length, and 10 cm in height.



(a) Mix of gelatin heating up



(b) Gelatin with the gap for the inclusion

Figure 3.3: Pictures from the preparation procedure of the gelatin phantoms. The picture from the left shows a mix with 15% gelatin concentration, which is poured in the gap from the gelatin in the right picture.

For the heterogeneous phantom, data acquired in [2] was used. An 8% gelatin concentration was chosen for the background and a 15% concentration for the inclusion. In the background, the same procedure was used to elaborate the homogeneous phantom, but with a plastic cylinder located 10 mm from the side of the container. This cylinder was later removed and the gap was filled with the 15% concentration mixture, as shown in Figure 3.3. In addition, mechanical measurements of the SWS were available, which were 3.45 m/s for the background and 5.1 m/s for the inclusion. These were taken with the time-of-flight method [2].

3.2.2 Equipment and protocol

The vibration sources were two shakers connected to a signal generator. Parallel plates were attached to each shaker and placed at each side of the phantom to transmit the vibration accordingly. The vibration frequencies went from 250 to 500 Hz in 50 Hz steps for the homogeneous phantoms, and from 200 to 360 Hz in 20 Hz steps for the heterogeneous phantoms. Lower frequencies were selected for the latter to address signal attenuation. In both cases, a 0.4 Hz difference in frequency was chosen for the generation of the interference pattern.

The ultrasound signal was generated using a 10 MHz pulse and a linear array with 128

elements, using a SonixTouch Research System. For the Doppler acquisition, a pulse repetition frequency of 1.7 kHz was set to avoid aliasing with the vibration sources, along with an ensemble size of 15 samples, which was the largest available. These settings were chosen based on the analysis carried out in [29].

The ultrasound scanner gives raw radio frequency signals, so an IQ (in-phase quadrature) demodulation process was performed. From the IQ signal, the B-mode image was obtained by calculating the envelope and converting it to decibels [1]. The sonoelastography signal is also obtained from the IQ data using the ensemble autocorrelation, as shown in the previous chapter, resulting in one sonoelastography frame for each ensemble [27][12]. This process is illustrated in Figure 3.4.

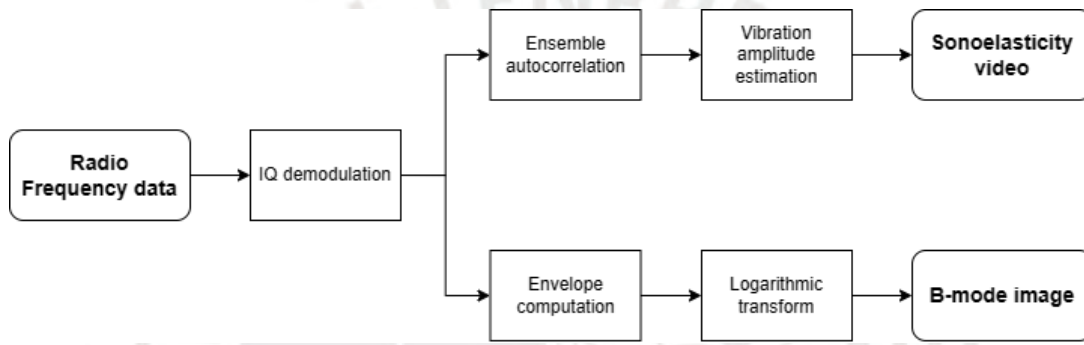


Figure 3.4: Flow diagram of the data acquisition process to obtain the B-mode images and the sonoelastography videos

3.2.3 Pre-processing

Three steps were performed before calculating the SWS image. First, a two-dimensional median filter was applied to each frame of the sonoelastography video for noise reduction. This filter was proposed in [34] to avoid salt-and-pepper noise. The kernel size was chosen so that it has the same length in the axial and lateral directions, about 0.9 mm. However, given that the lateral resolution (0.318 mm) differs from the axial resolution (0.101 mm), this results in a window length of 3 x 9 samples. For visualization purposes, a normalization step was performed for each depth by subtracting the mean and dividing the signal by its standard deviation. The results from these two steps are shown in Figure 3.5.

The last pre-processing step consists of applying a directional band-pass filter, to enhance the signal that would be obtained from shear velocities inside the previously mentioned range,

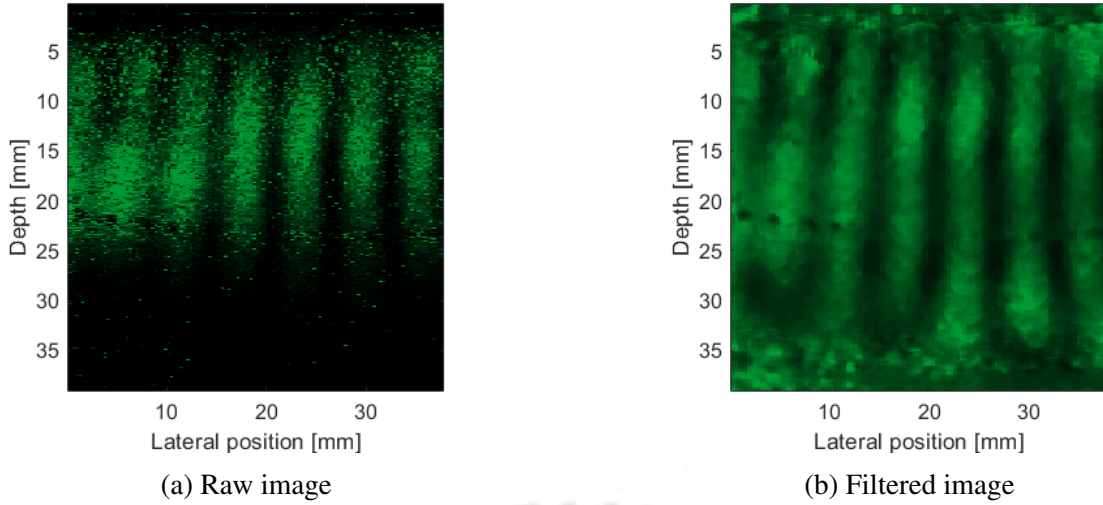


Figure 3.5: Sonoelastography pictures before and after applying the median filter and depth normalization. Images were generated with a vibration frequency of 350 Hz.

also proposed in [34]. This only requires the lateral and the slow-time dimension, so the same filter is applied for each depth slice. It was designed in the frequency domain by generating a mask of unit amplitude that is high when the temporal frequency is around the selected frequency offset for the generation of the Crawling Waves (0.4 Hz) and the shear wavelength is inside the expected range. This range varies depending on the vibration frequency, dictated by equation 2.24, so a different filter is used for each sonoelastography video. This mask is shown in 3.6(a). To avoid artifacts from reflections, the quadrant of the filter was selected taking into consideration the movement from the wave, left to right or right to left. This depends on which source is moving with a higher frequency. Afterward, the mask is convoluted with a Gaussian window to achieve a smooth frequency response, as shown in 3.6(b). Finally, the filter is implemented by direct multiplication in the frequency domain.

The effect of the directional filter can be observed in Figure 3.7. The image shows the sonoelastography signal obtained at a depth of 16 mm, with the x axis indicating lateral position and the y axis indicating time. In this case, the wave is moving from right to left.

3.3 Metrics

The objective is to assess the performance of the suggested SWS estimators, based on the STFT and the CWT in comparison to estimators currently in use. To achieve this, we have chosen

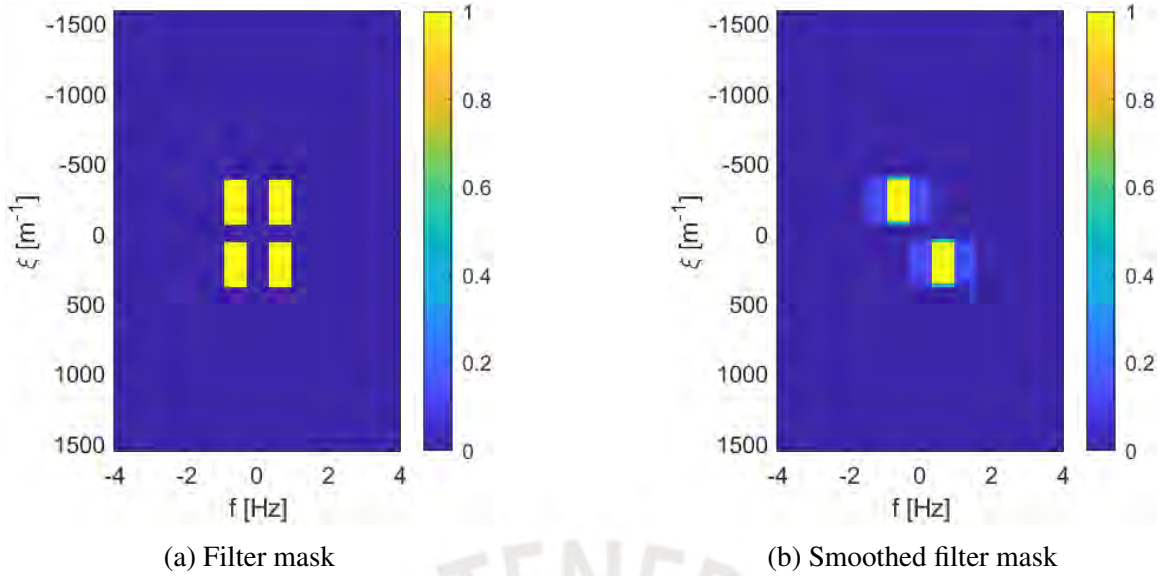


Figure 3.6: Directional filter on the frequency domain. The right image only includes two quadrants to enhance waves moving from right to left.

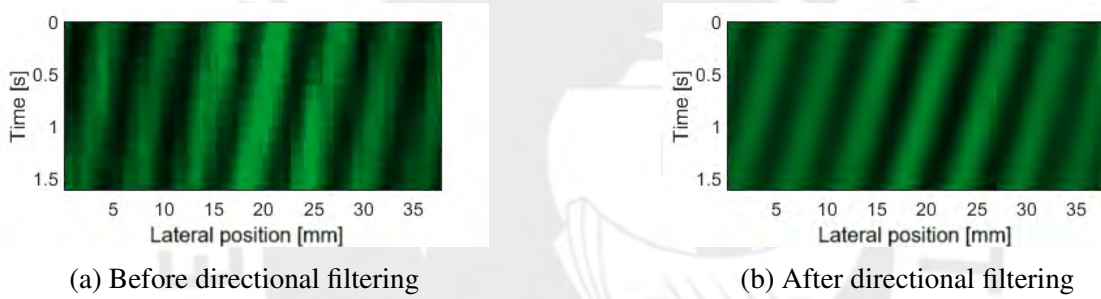


Figure 3.7: Effect of the directional filter in a sonoelastography signal generated at 350 Hz.

to compare it with PD and R-WAVE, previously described in the state-of-the-art section. We selected the former because it has been successfully implemented *in vivo* [3], and the latter due to its proven superiority over existing estimators [24]. The metrics and the regions of interest described subsequently are selected based on other comparative studies [45, 2].

For the homogeneous phantoms, a square region of interest was selected from the center of the image, such that the distance to the borders is larger than 5 mm. This was selected because reflections from the gelatin border create artifacts near the bottom and top of the image. All the samples from this region should have the same SWS, so the mean and standard deviation were calculated.

For the heterogeneous phantom, three regions were defined at the same depth: two in the background and one in the inclusion. The locations and sizes of these were chosen based on

the B-mode ultrasound image. The two background regions were rectangles of 10.8 mm x 5.4 mm, and the inclusion region was a square region with a side length of 10.8 mm. The regions were spaced 4 mm laterally. In Figure 3.8 the regions are shown on top of the B-mode image for the homogeneous and heterogeneous phantoms.

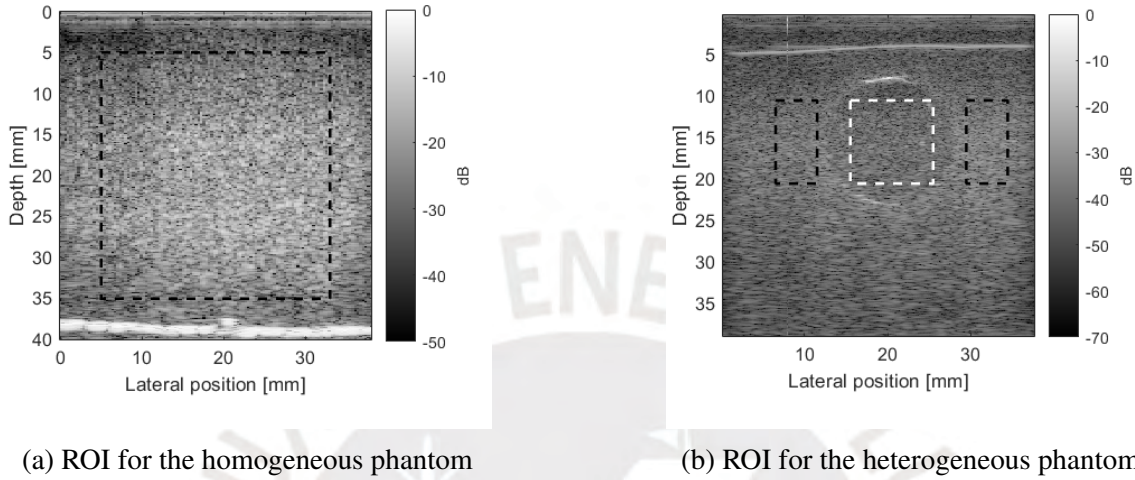


Figure 3.8: Regions of interest (ROI) on top of the B-mode ultrasound image for the homogeneous and heterogeneous phantoms.

The mean and standard deviation were calculated from all the samples within each region of interest, both spatially and in the time domain. Following that, the bias, Coefficient of Variation (CV), and the elastographic Contrast-to-Noise Ratio (CNR) [46] were calculated using the formulas in Equations 3.9, 3.10 and 3.11, where μ and σ denote the mean and standard deviation, respectively, of SWS measurements inside each region.

$$Bias = \frac{\mu - c_s}{\mu}, \quad (3.9)$$

$$CV = \frac{\sigma}{\mu}, \quad (3.10)$$

$$CNR = 20 \log_{10} \frac{2(\mu_{inc} - \mu_{back})}{\sigma_{inc}^2 + \sigma_{back}^2}. \quad (3.11)$$

The bias was only calculated for the heterogeneous phantoms, where ground-truth measurements were available. In addition, resolution is measured using the R_{2080} value, defined as the distance required for the SWS to change between the 20% and 80% of a transition zone between two interfaces, as in [45]. To accurately calculate this number, lateral

SWS lines between a 1 cm distance from the center of the inclusion were averaged to obtain a SWS line. This was fit to a double sigmoid curve defined by Equation 3.12, where c_0 and c_f are the mean SWS measured in the background and the inclusion, respectively, and x_1 and x_2 indicate the position of the left and right transitions between the two media.

$$c(x) = c_0 + (c_f - c_0) \left(\frac{1}{1 + e^{-(x-x_1)/\lambda_1}} \right) \left(\frac{1}{1 + e^{(x-x_2)/\lambda_2}} \right), \quad (3.12)$$

An illustration of this fit can be observed in Figure 3.9. Then, the resolution can be evaluated quantitatively with $R_{2080} = 2\lambda_i \ln 4$ [47]. Values from the left and right transition zones of the inclusion are averaged.

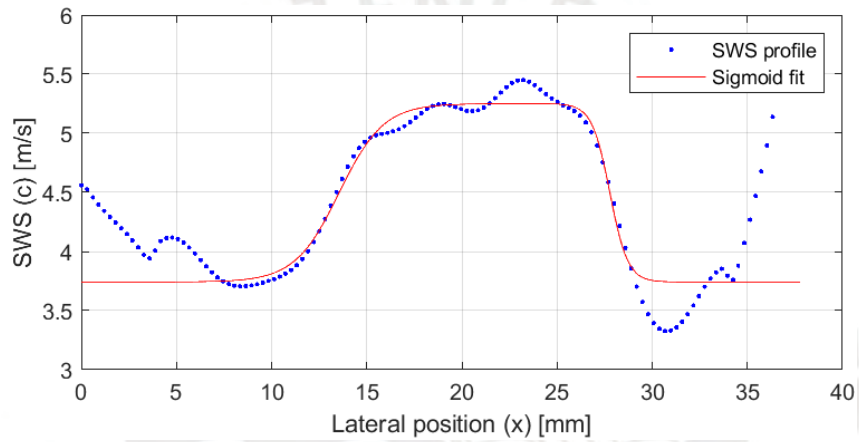


Figure 3.9: Averaged lateral profile of SWS measurements using PD and a sigmoid fit.

Chapter 4

Results

4.1 Homogeneous phantoms

The proposed algorithms, based on the STFT and the CWT were used to generate a SWS map for each vibration frequency. For displaying and comparison purposes, the mean value across all frames is computed and a single shear wave image is generated. The SWS maps generated for a vibration frequency of 400 Hz are shown on top of the B-mode image in Figure 4.1.

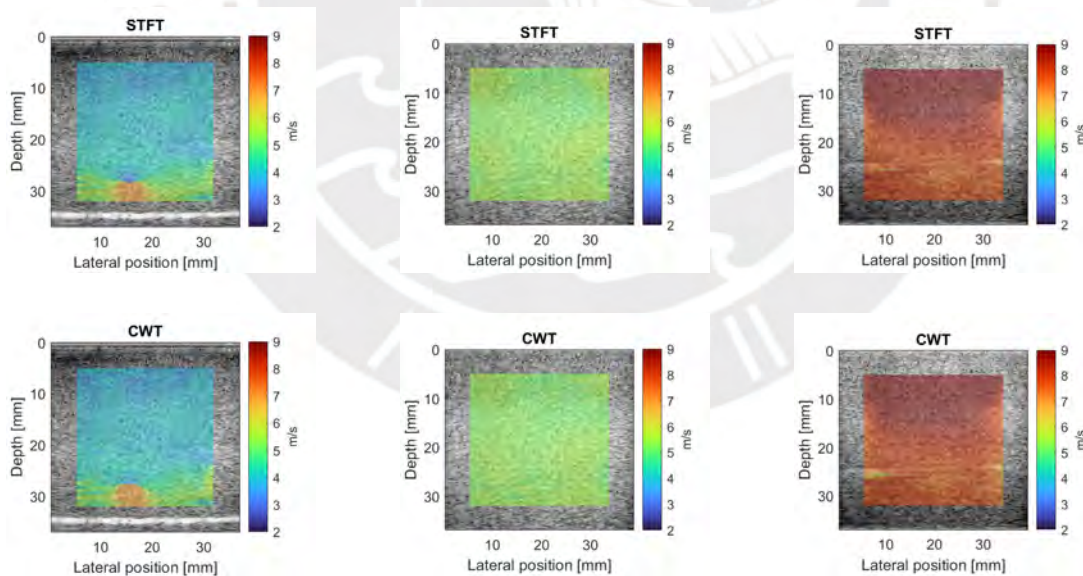


Figure 4.1: SWS maps on top of the B-mode ultrasound image obtained with a vibration frequency of 400 Hz. The left, middle, and right columns show the results for the phantoms with an 8%, 12%, and 20% gelatin concentration, respectively.

These maps correspond to a homogeneous medium and the estimated SWS goes according

to what is found in the literature, meaning a higher gelatin concentration corresponds to a higher SWS. Some artifacts can be observed at the bottom of the image in the 8% gelatin phantom and the 20% gelatin phantom. Nevertheless, they only occupy a small fraction of it for this particular case.

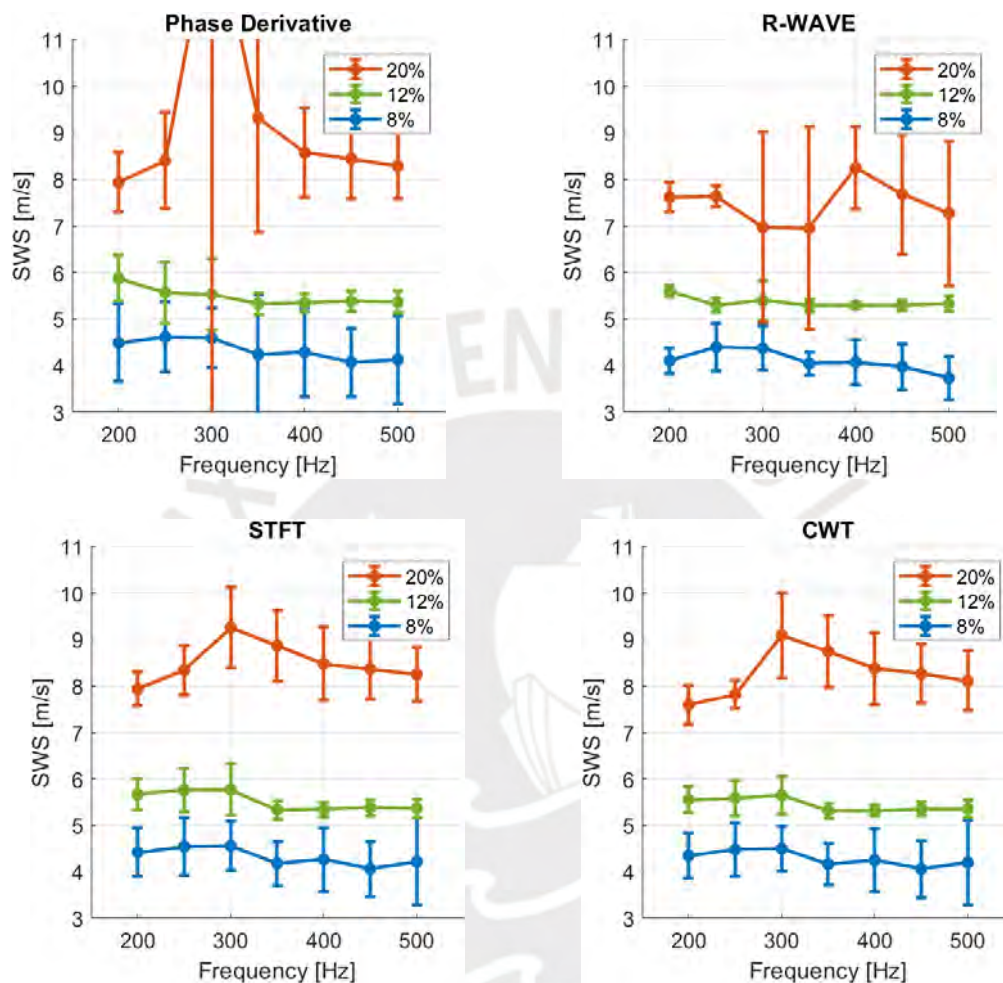


Figure 4.2: Mean SWS for each gelatin concentration. The limits for the vertical bars are given by the mean plus or minus the standard deviation.

Summarized results for vibration frequencies ranging from 200 Hz to 500 Hz are shown in Figure 4.2. The figure also shows results for two additional estimators available in the literature: PD [22] and R-WAVE [24]. A clear distinction in the shear speed can be observed for each gelatin concentration. No trend was found between SWS and vibration frequency, indicating the phantom does not exhibit viscoelastic behavior [8]. According to the figure, the proposed estimators have similar mean SWS across all samples and the results are consistent with the other two.

The CV can be observed in Figure 4.3. For the 8% and the 12% gelatin concentration phantom, R-WAVE has the lowest CV and PD the highest for almost all frequencies. Both the estimators based on the STFT and the CWT have similar performances, although the latter is slightly better. In the 20% gelatin phantom, PD has CV up to 90% for the 300 Hz sample. For vibration frequencies higher than 300 Hz, R-WAVE has a higher CV than both the STFT and the CWT, which remain under 10%.

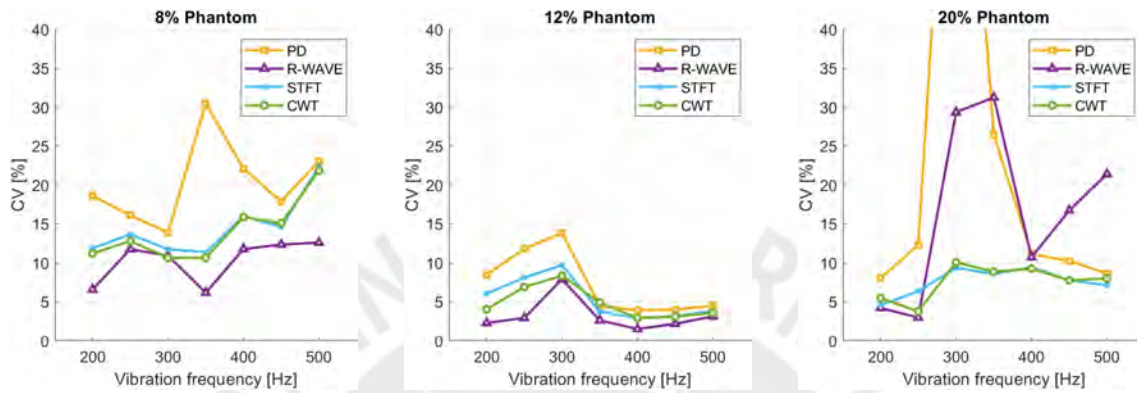


Figure 4.3: CV for all frequencies in the three manufactured gelatin phantoms, shown as a percentage

All results showed in the plots for the homogeneous phantoms are summarized in Table 4.1 for PD, Table 4.2 for R-WAVE, Table 4.3 for the STFT, and Table 4.4 for the CWT.

Gelatin concentration		Vibration Frequency [Hz]						
		200	250	300	350	400	450	500
20%	Mean [m/s]	7.94	8.40	13.77	9.32	8.57	8.44	8.29
	Std [m/s]	0.64	1.03	12.41	2.47	0.95	0.86	0.72
	CV [%]	8.03	12.30	90.10	26.46	11.12	10.23	8.63
12%	Mean [m/s]	5.88	5.57	5.53	5.33	5.34	5.38	5.36
	Std [m/s]	0.50	0.66	0.76	0.24	0.21	0.21	0.24
	CV [%]	8.44	11.79	13.82	4.48	3.88	3.98	4.50
8%	Mean [m/s]	4.49	4.61	4.59	4.24	4.29	4.07	4.13
	Std [m/s]	0.84	0.74	0.64	1.29	0.95	0.73	0.95
	CV [%]	18.59	16.09	13.88	30.45	22.06	17.88	23.05

Table 4.1: Results for PD in homogeneous phantoms

Gelatin concentration		Vibration Frequency [Hz]						
		200	250	300	350	400	450	500
20%	Mean [m/s]	7.61	7.64	6.97	6.95	8.24	7.68	7.27
	Std [m/s]	0.32	0.23	2.04	2.17	0.88	1.28	1.56
	CV [%]	4.19	2.96	29.33	31.25	10.72	16.72	21.40
12%	Mean [m/s]	5.60	5.30	5.40	5.29	5.29	5.30	5.32
	Std [m/s]	0.13	0.15	0.43	0.14	0.08	0.11	0.17
	CV [%]	2.27	2.92	7.89	2.61	1.48	2.16	3.11
8%	Mean [m/s]	4.11	4.40	4.37	4.04	4.07	3.98	3.73
	Std [m/s]	0.27	0.52	0.48	0.25	0.48	0.49	0.47
	CV [%]	6.56	11.74	10.90	6.15	11.77	12.33	12.60

Table 4.2: Results for R-WAVE in homogeneous phantoms

Gelatin concentration		Vibration Frequency [Hz]						
		200	250	300	350	400	450	500
20%	Mean [m/s]	7.94	8.34	9.26	8.87	8.48	8.37	8.25
	Std [m/s]	0.36	0.53	0.87	0.76	0.80	0.65	0.59
	CV [%]	4.58	6.33	9.35	8.56	9.44	7.75	7.12
12%	Mean [m/s]	5.67	5.76	5.77	5.34	5.34	5.38	5.36
	Std [m/s]	0.34	0.47	0.56	0.20	0.15	0.17	0.20
	CV [%]	6.02	8.10	9.68	3.75	2.87	3.16	3.79
8%	Mean [m/s]	4.42	4.55	4.56	4.18	4.26	4.07	4.22
	Std [m/s]	0.53	0.62	0.54	0.48	0.68	0.59	0.95
	CV [%]	11.87	13.65	11.73	11.36	16.02	14.59	22.40

Table 4.3: Results for the STFT in homogeneous phantoms

Gelatin concentration		Vibration Frequency [Hz]						
		200	250	300	350	400	450	500
20%	Mean [m/s]	7.59	7.82	9.10	8.75	8.38	8.26	8.11
	Std [m/s]	0.41	0.29	0.91	0.77	0.77	0.64	0.65
	CV [%]	5.46	3.77	10.05	8.86	9.24	7.74	8.00
12%	Mean [m/s]	5.58	5.73	5.67	5.35	5.33	5.32	5.34
	Std [m/s]	0.23	0.39	0.47	0.26	0.15	0.16	0.19
	CV [%]	4.03	6.88	8.33	4.87	2.89	3.10	3.56
8%	Mean [m/s]	4.35	4.48	4.50	4.17	4.25	4.06	4.20
	Std [m/s]	0.49	0.57	0.48	0.44	0.67	0.61	0.92
	CV [%]	11.18	12.78	10.64	10.66	15.87	15.09	21.85

Table 4.4: Results for the CWT in homogeneous phantoms

4.2 Heterogeneous phantoms

As with the homogeneous phantoms, SWS maps for all frequencies were generated using the previously mentioned estimators. The mean value across all frames was used to generate the images using the STFT and the CWT. A representative result is presented in Figure 4.4. The SWS map is overlapped on top of the B-mode ultrasound. These results are consistent and the harder inclusion can be easily recognized in all images, although some artifacts can be observed at the top part. The SWS map generated via PD seems to be more noisy in comparison with the others, especially in the inclusion.

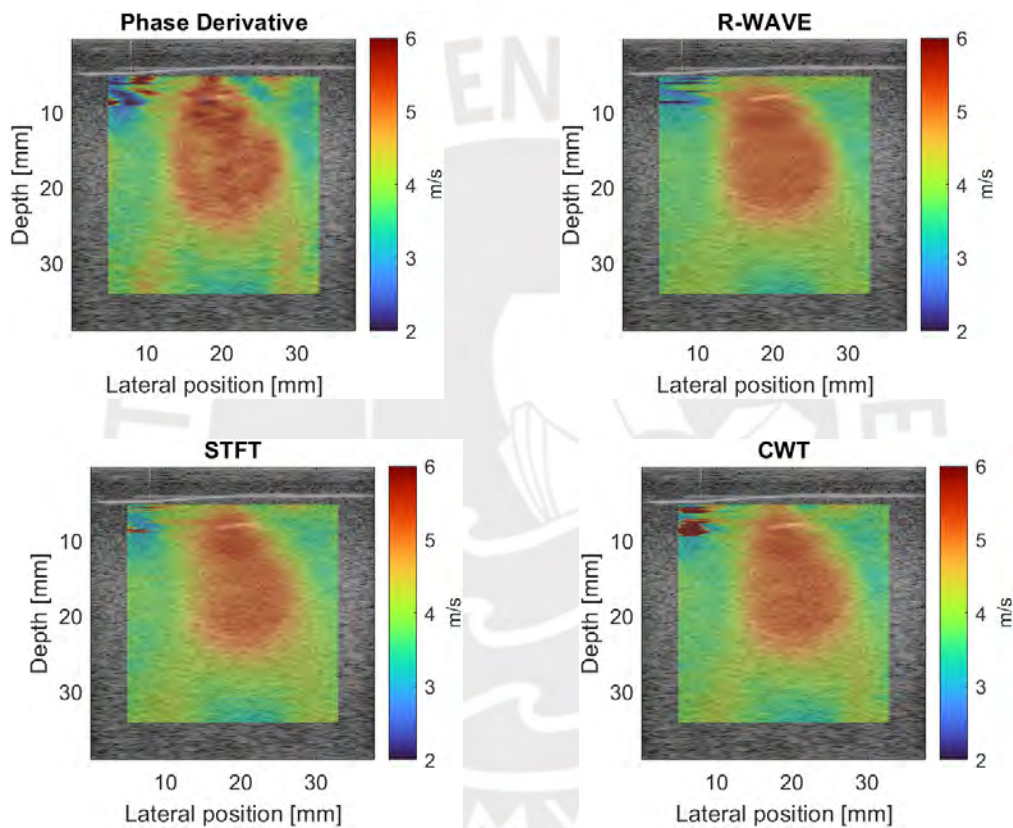


Figure 4.4: SWS maps overlaid on top of B-mode images for each method from sonoelastography data obtained at a vibration frequency of 340 Hz.

Results for several frequencies are summarized in Figure 4.5. In all the generated images there is a clear distinction between the SWS in the inclusion and the background. In addition, the mean SWS with the four estimators does not correlate with vibration frequency, as expected for non-viscoelastic materials [8].

The PD method is the one with the greatest standard deviation, as in the homogeneous data.

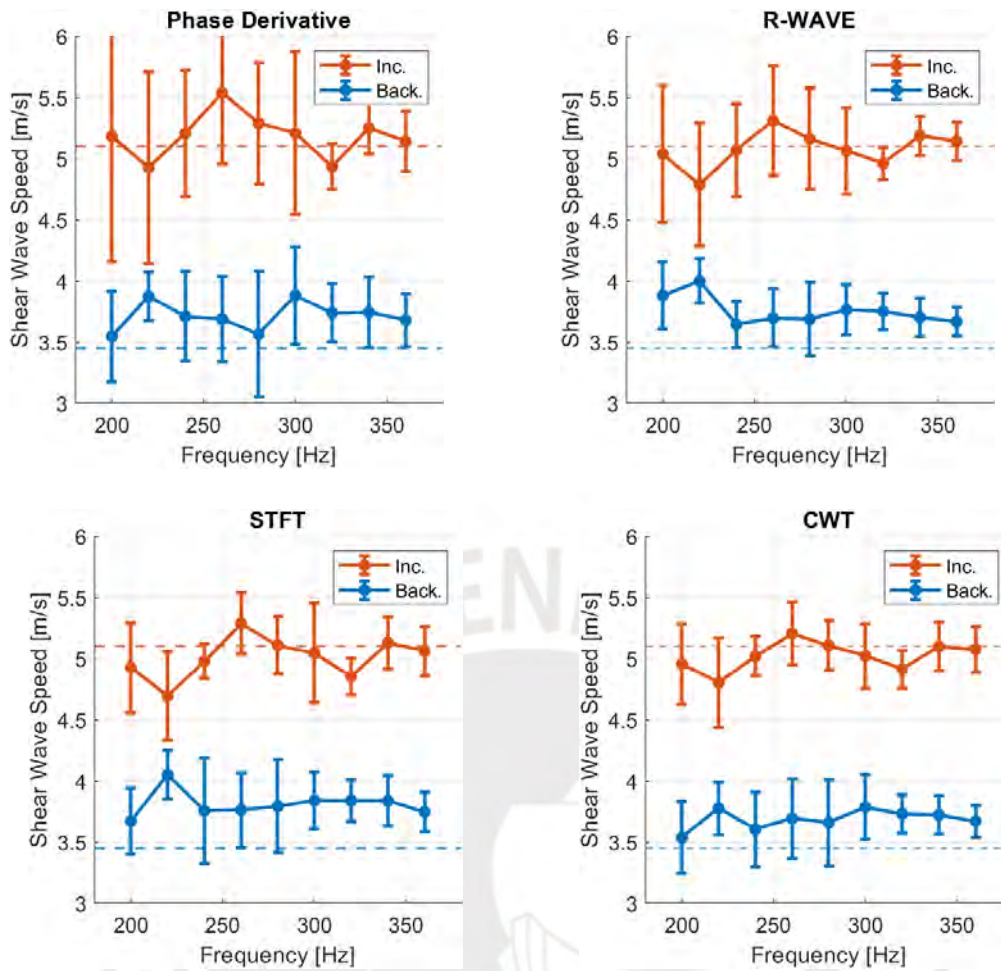


Figure 4.5: Mean SWS and standard deviation at several frequencies from the assessed SWS estimators. The dotted lines indicate the ground-truth SWS.

This is reflected in the CV, shown in Figure 4.6. Taking into account all vibration frequencies, the average CV with PD is 10.1% for the inclusion and 8.1% for the background, whereas with CWT is 4.7% for the inclusion and 6.7% for the background. At frequencies lower than 300 Hz, the two proposed algorithms based on the CWT and the STFT exhibit lower variation in the inclusion than R-WAVE and PD.

For the bias, displayed in Figure 4.7, similar results for the estimators can be observed. In the inclusion, PD has the highest bias on average, which is 7.6%, and the STFT has the lowest negative bias, which is -1.8%. In the background, all estimators have a positive bias, meaning they estimate a higher SWS, reaching values greater than 15%. The STFT seems to have a more positive bias, which is 10.4% on average, and the rest of the estimators have similar performances.

The CNR, displayed in Figure 4.8 is also of high relevance. CWT and R-WAVE have a

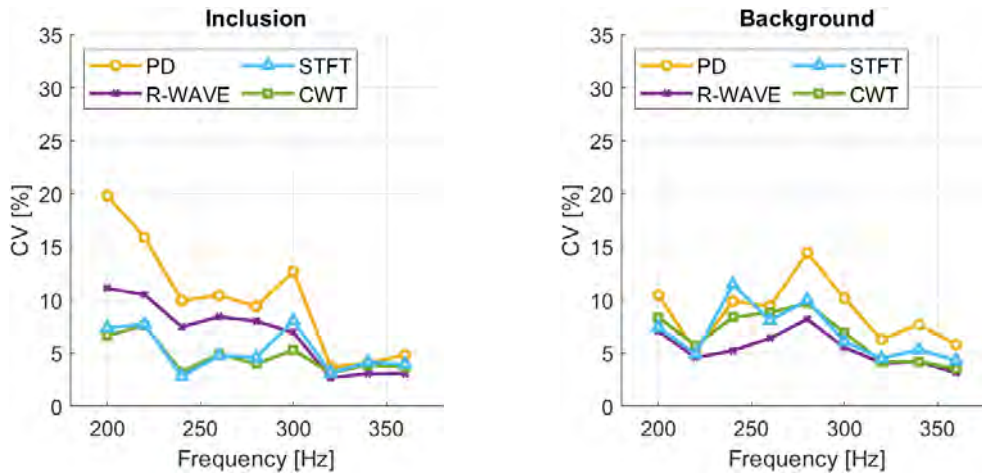


Figure 4.6: CV for all frequencies in the inclusion and the background of the heterogeneous phantom, shown as a percentage

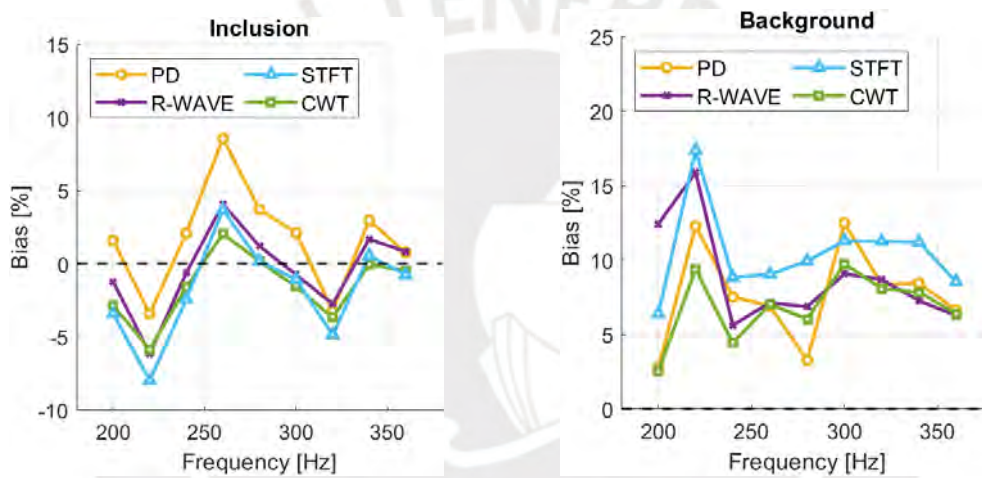


Figure 4.7: Bias for all frequencies in the inclusion and the background of the heterogeneous phantom, shown as a percentage

higher CNR than the other two estimators, reaching almost 40 dB at 360 Hz. PD has the worst CNR, with a minimum of 10 dB at 220 Hz. On average, the mean CNR of each estimator was 21.8 dB for PD, 27.7 dB for R-WAVE, 30 dB for CWT, and 26.2 dB for STFT. The estimator based on the CWT has a higher CNR than the one based on the STFT in almost all frequencies. In addition, an overall upward trend with frequency can be observed in all estimators.

Lastly, resolution, as defined in the previous chapter, is shown in Figure 4.8. PD had the lowest R_{2080} values from most frequencies, meaning that a sharper image border can be captured (average is 1.76 mm). On the contrary, the STFT approach had the largest R_{2080} in five out of nine frequencies, averaging 2.93 mm. In addition, a clear trend can be observed for the CWT, where higher vibration frequencies correspond to a sharper resolution.

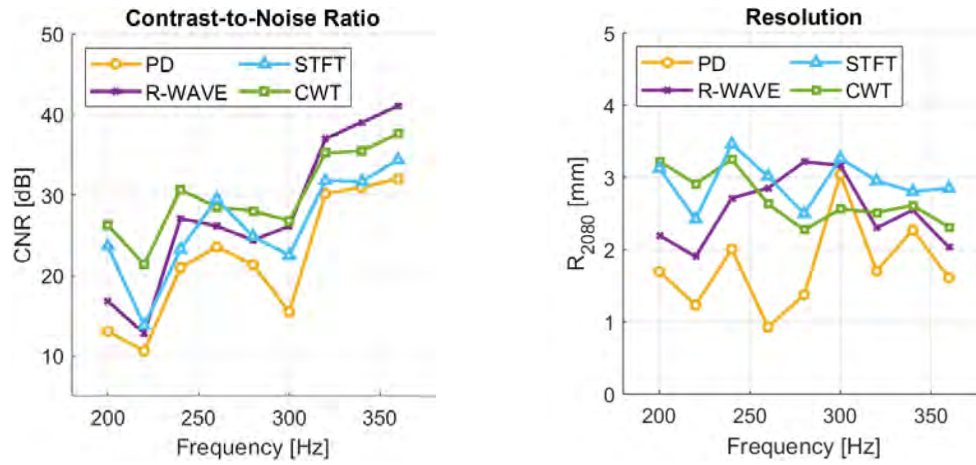


Figure 4.8: CNR and resolution for all frequencies of the heterogeneous phantom

Numerical values of the mean, standard deviation, CV, and bias for each region and each vibration frequency are displayed in Table 4.5 for PD, Table 4.6 for R-WAVE, Table 4.7 for the STFT, and Table 4.8 for the CWT.

ROI		Vibration Frequency [Hz]								
		200	220	240	260	280	300	320	340	360
Inclusion	Mean [m/s]	5.18	4.93	5.21	5.54	5.29	5.21	4.94	5.25	5.14
	Std [m/s]	1.03	0.78	0.52	0.58	0.50	0.66	0.18	0.21	0.25
	CV [%]	19.82	15.90	9.94	10.44	9.40	12.71	3.71	4.08	4.83
	Bias [%]	1.59	-3.40	2.10	8.56	3.70	2.13	-3.21	2.96	0.77
Background	Mean [m/s]	3.55	3.87	3.71	3.69	3.56	3.88	3.74	3.74	3.68
	Std [m/s]	0.37	0.20	0.37	0.35	0.51	0.39	0.24	0.29	0.21
	CV [%]	10.46	5.21	9.88	9.42	14.44	10.17	6.30	7.71	5.82
	Bias [%]	2.80	12.28	7.53	6.92	3.28	12.49	8.38	8.47	6.64

Table 4.5: Results for PD in heterogeneous phantom

ROI		Vibration Frequency [Hz]								
		200	220	240	260	280	300	320	340	360
Inclusion	Mean [m/s]	5.04	4.79	5.07	5.31	5.16	5.06	4.96	5.19	5.14
	Std [m/s]	0.56	0.50	0.38	0.45	0.41	0.35	0.13	0.16	0.16
	CV [%]	11.11	10.50	7.49	8.44	8.02	6.96	2.70	3.07	3.10
	Bias [%]	-1.21	-6.13	-0.61	4.09	1.20	-0.73	-2.74	1.69	0.82
Background	Mean [m/s]	3.88	4.00	3.64	3.70	3.69	3.76	3.75	3.70	3.67
	Std [m/s]	0.27	0.18	0.19	0.24	0.30	0.21	0.15	0.16	0.12
	CV [%]	7.08	4.56	5.23	6.41	8.22	5.52	4.08	4.20	3.14
	Bias [%]	12.44	15.88	5.64	7.14	6.87	9.08	8.71	7.27	6.28

Table 4.6: Results for R-WAVE in heterogeneous phantom

ROI		Vibration Frequency [Hz]								
		200	220	240	260	280	300	320	340	360
Inclusion	Mean [m/s]	4.93	4.69	4.98	5.29	5.11	5.05	4.85	5.13	5.06
	Std [m/s]	0.37	0.36	0.14	0.25	0.24	0.41	0.15	0.21	0.20
	CV [%]	7.41	7.72	2.83	4.77	4.60	8.04	3.15	4.16	3.96
	Bias [%]	-3.40	-7.96	-2.40	3.67	0.18	-1.05	-4.85	0.57	-0.75
Background	Mean [m/s]	3.67	4.05	3.76	3.76	3.79	3.84	3.84	3.84	3.75
	Std [m/s]	0.27	0.20	0.43	0.30	0.38	0.23	0.17	0.20	0.16
	CV [%]	7.45	4.92	11.49	8.08	9.98	6.09	4.49	5.33	4.32
	Bias [%]	6.40	17.35	8.84	9.06	9.94	11.29	11.27	11.21	8.56

Table 4.7: Results for the STFT in heterogeneous phantom

ROI		Vibration Frequency [Hz]								
		200	220	240	260	280	300	320	340	360
Inclusion	Mean [m/s]	4.96	4.80	5.02	5.20	5.11	5.02	4.91	5.10	5.07
	Std [m/s]	0.33	0.37	0.16	0.26	0.20	0.27	0.15	0.20	0.19
	CV [%]	6.66	7.62	3.24	4.92	4.00	5.29	3.15	3.90	3.70
	Bias [%]	-2.83	-5.83	-1.59	2.06	0.16	-1.54	-3.66	-0.04	-0.50
Background	Mean [m/s]	3.54	3.77	3.60	3.69	3.66	3.79	3.73	3.72	3.67
	Std [m/s]	0.30	0.22	0.30	0.33	0.35	0.26	0.16	0.16	0.13
	CV [%]	8.38	5.75	8.39	8.84	9.69	6.95	4.21	4.20	3.54
	Bias [%]	2.53	9.40	4.46	7.02	6.05	9.76	8.10	7.86	6.39

Table 4.8: Results for the CWT in heterogeneous phantom

4.3 SWS from a single frame

The developed estimators can generate a SWS map from a single sonoelastography frame. To assess the possibility of implementing them in real time, their accuracy must be tested when obtaining a single SWS image without the directional filter, which involves the use of many frames. Some resulting SWS images can be observed in Figure 4.9.

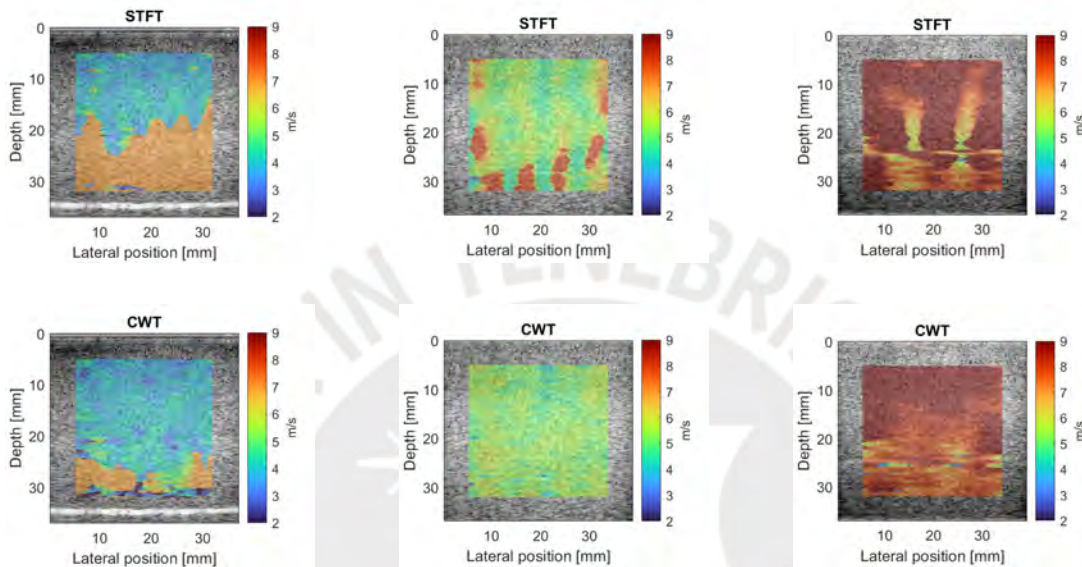


Figure 4.9: SWS maps on top of the B-mode ultrasound image obtained with a vibration frequency of 400 Hz from a single sonoelastography frame and no directional filtering. The left, middle, and right columns show the results for the phantoms with an 8%, 12%, and 20% gelatin concentration, respectively.

Results from all vibration frequencies are shown in Figure 4.10. The mean SWS is still distinct for each gelatin concentration and the dispersion is comparable to the estimators that use the whole set of frames (PD and R-WAVE).

4.4 Discussion

Homogeneous phantom experiments were performed and the performance of the proposed algorithms, based on the STFT and the CWT, was evaluated. In terms of the CV, both estimators show similar performance. This behavior is expected given that both estimators work with the same principle, which is space-frequency decomposition. Results are comparable with estimators in the state of the art (PD and R-WAVE). In the 20% gelatin

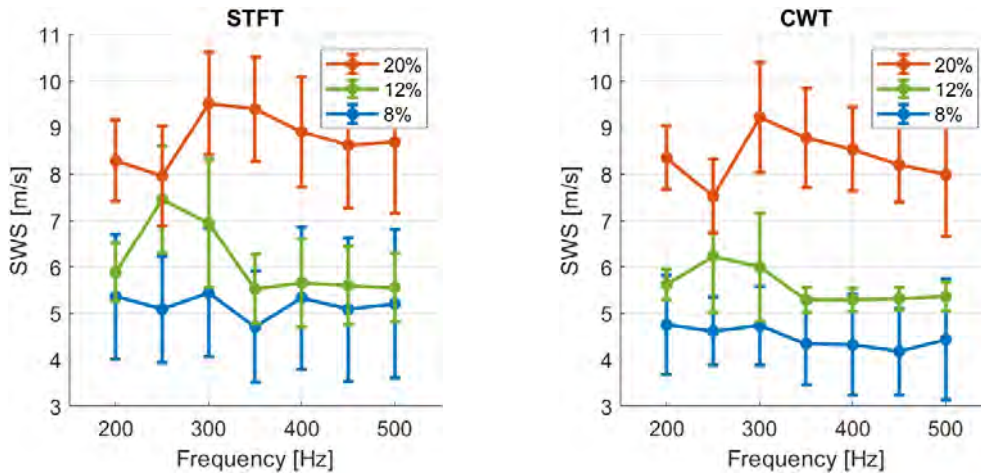


Figure 4.10: Mean SWS for each gelatin concentration. The limits for the vertical bars are given by the mean plus or minus the standard deviation.

concentration phantom, it can be appreciated that the SWS exhibits an abnormally high variation with PD and R-WAVE, with different mean values when comparing results from other frequencies and a higher CV. Results from the proposed estimators are most consistent.

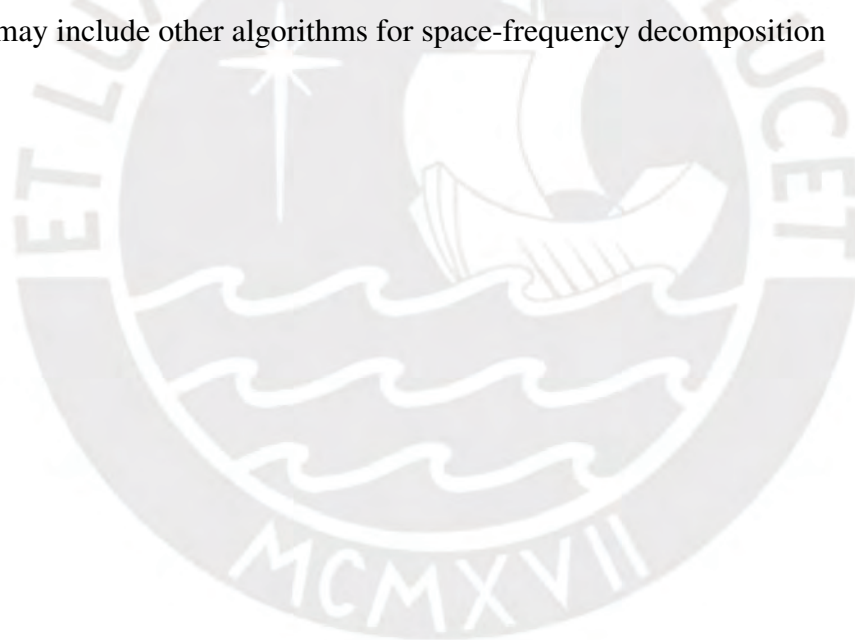
Two possible causes for the improvement were identified. The first one is that higher stiffness of the tissue leads to increased attenuation of the shear waves, resulting in a diminished signal-to-noise ratio. This issue has a major impact on the images generated by PD, which is more sensitive to noise due to its nature because differentiation intrinsically amplifies noise. This observation is supported by the results for the CV, which showed higher results in almost all cases for PD, as shown in Table 4.1. The second cause is that a higher SWS implies that a longer wavelength is generated. R-WAVE is based on the measurement of the wavelengths in the spatial domain through a peak detection algorithm. Longer wavelengths can be problematic for the algorithm, leading to potential errors [24].

The results with the heterogeneous phantom are also consistent with what was previously mentioned. PD and R-WAVE give more spread-out results in the inclusion, which has a higher SWS. This is reflected in the CV, especially at lower frequencies, as shown in Tables 4.5 and 4.6.

According to the results from the bias, the STFT overestimates the SWS in the background and underestimates it in the inclusion more than the other estimators. This can happen due to low resolution: longer wavelengths require longer windows, which decreases spatial resolution. However, the CWT is less affected by these effects, because it employs wavelets that can adapt

their size to match the local frequency content of the signal. This flexibility allows the CWT to achieve better frequency resolution for high-frequency components and better time resolution for low-frequency components simultaneously. This is also the reason why it has a higher CNR ratio than the STFT. Measurements of R_{2080} also confirm the higher resolution that can be achieved with CWT when using higher vibration frequencies.

Lastly, one of the most notable features of the proposed algorithms is they can still be applied in one dimension. In Figure 4.9, some artifacts can be seen in the image generated by the STFT, but the CWT gives more accurate results. In general, across most frequencies, the CWT allows the generation of images with low dispersion in the region of interest even without filtering. This implies that a SWS map can be generated from a single sonoelastography frame with this technique, an achievement that other methods in the literature were unable to attain. As a consequence, the visualization of a SWS map in real time could be possible when using this method, as compared with the other algorithms, which usually need more information. Future work may include other algorithms for space-frequency decomposition



Conclusions

- The results of the experiments conducted in gelatin homogeneous phantoms confirmed the successful implementation of the algorithms. The average SWS was inside the desired range, from 2 to 9 m/s, and the proposed algorithms demonstrated an average coefficient of variation lower than 10%, surpassing the performance of estimators found in current literature.
- In the heterogeneous phantoms, the bias, CV, and resolution showed similar performance of the proposed algorithms compared to the existing ones. This confirms their reliability and accuracy in estimating shear wave speed. The CWT achieved a higher CNR than the other analyzed estimators, reaching 30 dB on average, which indicates that it allows better discrimination of regions with different shear wave speeds.
- The robustness of the implemented algorithms was assessed in challenging scenarios with noisy sonoelastography data and higher shear wave speeds. The algorithms exhibited a higher CNR and a lower CV under these conditions, indicating that they are more robust.

Recommendations

- The algorithm based on the CWT is recommended over the STFT, due to its superior performance on average in terms of CNR and resolution.
- The implemented algorithms address the limitation of needing several sonoelastography frames and are recommended for real-time visualization of SWS images. This would provide valuable feedback to the operator during the acquisition process, facilitating its use in clinical applications.
- The completion of this research highlights the potential of Crawling Waves Sonoelastography as a valuable technique for the non-invasive assessment of tissue elasticity. The proposed algorithms contribute to the advancement of this field by providing reliable and robust shear wave speed estimation, which is crucial for various clinical applications such as tumor detection, liver fibrosis staging, and musculoskeletal tissue evaluation.
- Future studies should be focused on evaluating new estimators based on a single sonoelasticity frame value, real-time implementation, and tissue characterization.

Bibliography

- [1] P. R. Hoskins, K. Martin, and A. Thrush, *Diagnostic ultrasound: physics and equipment*. CRC Press, 2019.
- [2] S. E. Romero, E. A. Gonzalez, R. Lavarello, and B. Castañeda, “A comparative study between parallel and normal excitation for crawling wave sonoelastography,” in *12th International Symposium on Medical Information Processing and Analysis*, vol. 10160, pp. 428–435, SPIE, 2017.
- [3] E. A. Gonzalez, S. E. Romero, and B. Castaneda, “Real-time crawling wave sonoelastography for human muscle characterization: Initial results,” *IEEE transactions on ultrasonics, ferroelectrics, and frequency control*, vol. 66, no. 3, pp. 563–571, 2018.
- [4] T. L. Szabo, *Diagnostic ultrasound imaging: inside out*. Academic press, 2004.
- [5] G. Xiao, S. Zhu, X. Xiao, L. Yan, J. Yang, and G. Wu, “Comparison of laboratory tests, ultrasound, or magnetic resonance elastography to detect fibrosis in patients with nonalcoholic fatty liver disease: a meta-analysis,” *Hepatology*, vol. 66, no. 5, pp. 1486–1501, 2017.
- [6] G. Sadigh, R. C. Carlos, C. H. Neal, and B. A. Dwamena, “Accuracy of quantitative ultrasound elastography for differentiation of malignant and benign breast abnormalities: a meta-analysis,” *Breast cancer research and treatment*, vol. 134, no. 3, pp. 923–931, 2012.
- [7] R. Prado-Costa, J. Rebelo, J. Monteiro-Barroso, and A. S. Preto, “Ultrasound elastography: compression elastography and shear-wave elastography in the assessment of tendon injury,” *Insights into imaging*, vol. 9, no. 5, pp. 791–814, 2018.

- [8] I. Z. Nenadic, M. W. Urban, J. F. Greenleaf, J.-L. Gennisson, M. Bernal, and M. Tanter, *Ultrasound elastography for biomedical applications and medicine*. Wiley Online Library, 2019.
- [9] J. Ormachea and K. Parker, “Elastography imaging: the 30 year perspective,” *Physics in Medicine & Biology*, vol. 65, no. 24, p. 24TR06, 2020.
- [10] G. Montaldo, M. Tanter, J. Bercoff, N. Benech, and M. Fink, “Coherent plane-wave compounding for very high frame rate ultrasonography and transient elastography,” *IEEE transactions on ultrasonics, ferroelectrics, and frequency control*, vol. 56, no. 3, pp. 489–506, 2009.
- [11] Z. Wu, L. S. Taylor, D. J. Rubens, and K. J. Parker, “Sonoelastographic imaging of interference patterns for estimation of the shear velocity of homogeneous biomaterials,” *Physics in Medicine & Biology*, vol. 49, no. 6, p. 911, 2004.
- [12] S.-R. Huang, R. M. Lerner, and K. J. Parker, “On estimating the amplitude of harmonic vibration from the doppler spectrum of reflected signals,” *The Journal of the Acoustical Society of America*, vol. 88, no. 6, pp. 2702–2712, 1990.
- [13] J. Walsh, L. An, B. Mills, Z. Hah, J. Moalem, M. Miller, E. Giampoli, K. Parker, and D. Rubens, “Quantitative crawling wave sonoelastography of benign and malignant thyroid nodules,” *Otolaryngology–Head and Neck Surgery*, vol. 147, no. 2, pp. 233–238, 2012.
- [14] K. Hoyt, B. Castaneda, M. Zhang, P. Nigwekar, P. A. di Sant’Agnese, J. V. Joseph, J. Strang, D. J. Rubens, and K. J. Parker, “Tissue elasticity properties as biomarkers for prostate cancer,” *Cancer Biomarkers*, vol. 4, no. 4-5, pp. 213–225, 2008.
- [15] C. T. Barry, B. Mills, Z. Hah, R. A. Mooney, C. K. Ryan, D. J. Rubens, and K. J. Parker, “Shear wave dispersion measures liver steatosis,” *Ultrasound in medicine & biology*, vol. 38, no. 2, pp. 175–182, 2012.
- [16] A. C. Saavedra, B. Castaneda, and R. J. Lavarello, “Multi-wave dermis characterization using attenuation coefficient and shear wave speed estimates in vivo,” in *2019 IEEE International Ultrasonics Symposium (IUS)*, pp. 1269–1272, IEEE, 2019.

- [17] Z. Wu, K. Hoyt, D. J. Rubens, and K. J. Parker, “Sonoelastographic imaging of interference patterns for estimation of shear velocity distribution in biomaterials,” *The Journal of the Acoustical Society of America*, vol. 120, no. 1, pp. 535–545, 2006.
- [18] H. Knutsson, C.-F. Westin, and G. H. Granlund, “Local multiscale frequency and bandwidth estimation.,” in *ICIP (1)*, pp. 36–40, 1994.
- [19] A. Manduca, R. Muthupillai, P. J. Rossman, J. F. Greenleaf, and R. L. Ehman, “Image processing for magnetic-resonance elastography,” in *Medical Imaging 1996: Image Processing*, vol. 2710, pp. 616–623, SPIE, 1996.
- [20] K. Hoyt, K. J. Parker, and D. J. Rubens, “Real-time shear velocity imaging using sonoelastographic techniques,” *Ultrasound in medicine & biology*, vol. 33, no. 7, pp. 1086–1097, 2007.
- [21] K. Hoyt, B. Castaneda, and K. J. Parker, “Two-dimensional sonoelastographic shear velocity imaging,” *Ultrasound in medicine & biology*, vol. 34, no. 2, pp. 276–288, 2008.
- [22] Z. Hah, C. Hazard, B. Mills, C. Barry, D. Rubens, and K. Parker, “Integration of crawling waves in an ultrasound imaging system. part 2: signal processing and applications,” *Ultrasound in medicine & biology*, vol. 38, no. 2, pp. 312–323, 2012.
- [23] E. A. Gonzalez, J. Ormachea, K. J. Parker, and B. Castaneda, “Wavelength average velocity estimator for ultrasound elastography,” in *2016 IEEE 13th International Symposium on Biomedical Imaging (ISBI)*, pp. 1017–1020, IEEE, 2016.
- [24] E. González, P. Li, J. Ormachea, K. Parker, R. Lavarello, and B. Castañeda, “Regularized wavelength average velocity estimator for quantitative ultrasound elastography,” in *2016 IEEE International Ultrasonics Symposium (IUS)*, pp. 1–4, IEEE, 2016.
- [25] S. Merino, B. Castaneda, and S. E. Romero, “Shear wave speed estimation for crawling wave sonoelastography using the short-time fourier transform,” in *2021 IEEE International Ultrasonics Symposium (IUS)*, pp. 1–4, IEEE, 2021.
- [26] S. Merino, S. E. Romero, E. A. Gonzalez, and B. Castaneda, “Shear wave speed estimator using continuous wavelet transform for crawling wave sonoelastography,” in *2021 43rd*

Annual International Conference of the IEEE Engineering in Medicine & Biology Society (EMBC), pp. 3994–3997, IEEE, 2021.

- [27] C. Kasai, K. Namekawa, A. Koyano, and R. Omoto, “Real-time two-dimensional blood flow imaging using an autocorrelation technique,” *IEEE Transactions on sonics and ultrasonics*, vol. 32, no. 3, pp. 458–464, 1985.
- [28] L. Taylor, B. Porter, D. J. Rubens, and K. Parker, “Three-dimensional sonoelastography: principles and practices,” *Physics in Medicine & Biology*, vol. 45, no. 6, p. 1477, 2000.
- [29] G. Torres Gárate, “Caracterización de un ecógrafo de investigación para aplicaciones en sonoelastografía,”
- [30] K. J. Parker, L. S. Taylor, S. Gracewski, and D. J. Rubens, “A unified view of imaging the elastic properties of tissue,” *The Journal of the Acoustical Society of America*, vol. 117, no. 5, pp. 2705–2712, 2005.
- [31] K. J. Parker, M. M. Doyley, and D. J. Rubens, “Imaging the elastic properties of tissue: the 20 year perspective,” *Physics in medicine & biology*, vol. 56, no. 1, p. R1, 2010.
- [32] R. Rojas, J. Ormachea, A. Salo, P. Rodríguez, K. J. Parker, and B. Castaneda, “Crawling waves speed estimation based on the dominant component analysis paradigm,” *Ultrasonic imaging*, vol. 37, no. 4, pp. 341–355, 2015.
- [33] D.-Y. Liu, O. Gibaru, and W. Perruquetti, “Error analysis of jacobi derivative estimators for noisy signals,” *Numerical Algorithms*, vol. 58, no. 1, pp. 53–83, 2011.
- [34] B. Castaneda, L. An, S. Wu, L. L. Baxter, J. L. Yao, J. V. Joseph, K. Hoyt, J. Strang, D. J. Rubens, and K. J. Parker, “Prostate cancer detection using crawling wave sonoelastography,” in *Medical Imaging 2009: Ultrasonic Imaging and Signal Processing*, vol. 7265, pp. 338–347, SPIE, 2009.
- [35] L. Cohen, *Time-frequency analysis*, vol. 778. Prentice Hall PTR New Jersey, 1995.
- [36] M. H. Hayes, *Statistical digital signal processing and modeling*. John Wiley & Sons, 1996.

- [37] L. Chun-Lin, “A tutorial of the wavelet transform,” *NTUET, Taiwan*, vol. 21, no. 22, p. 2, 2010.
- [38] J. M. Lilly, “Element analysis: a wavelet-based method for analysing time-localized events in noisy time series,” *Proceedings of the Royal Society A: Mathematical, Physical and Engineering Sciences*, vol. 473, no. 2200, p. 20160776, 2017.
- [39] S. Stanković, I. Orović, and E. Sejdić, *Multimedia signals and systems*. Springer, 2012.
- [40] R. M. Sigrist, J. Liau, A. El Kaffas, M. C. Chammas, and J. K. Willmann, “Ultrasound elastography: review of techniques and clinical applications,” *Theranostics*, vol. 7, no. 5, p. 1303, 2017.
- [41] J. M. Lilly and S. C. Olhede, “On the analytic wavelet transform,” *IEEE transactions on information theory*, vol. 56, no. 8, pp. 4135–4156, 2010.
- [42] T. M. Inc., “Wavelet toolbox version: 6.3 (r2023a),” 2023.
- [43] J. M. Lilly and S. C. Olhede, “Generalized morse wavelets as a superfamily of analytic wavelets,” *IEEE Transactions on Signal Processing*, vol. 60, no. 11, pp. 6036–6041, 2012.
- [44] A. C. Saavedra Bazán, *Comparación de técnicas de elastografía cuantitativa basadas en vibración mecánica externa en equipos ultrasónicos de investigación con diferentes rangos de frecuencia*. PhD thesis, Pontificia Universidad Católica del Perú, Facultad de Ciencias e Ingeniería, 2015.
- [45] J. Ormachea, R. J. Lavarello, S. A. McAleavey, K. J. Parker, and B. Castaneda, “Shear wave speed measurements using crawling wave sonoelastography and single tracking location shear wave elasticity imaging for tissue characterization,” *IEEE transactions on ultrasonics, ferroelectrics, and frequency control*, vol. 63, no. 9, pp. 1351–1360, 2016.
- [46] T. Varghese and J. Ophir, “An analysis of elastographic contrast-to-noise ratio,” *Ultrasound in medicine & biology*, vol. 24, no. 6, pp. 915–924, 1998.
- [47] N. C. Rouze, M. H. Wang, M. L. Palmeri, and K. R. Nightingale, “Parameters affecting the resolution and accuracy of 2-d quantitative shear wave images,” *IEEE transactions on ultrasonics, ferroelectrics, and frequency control*, vol. 59, no. 8, pp. 1729–1740, 2012.